We are IntechOpen, the world's leading publisher of Open Access books Built by scientists, for scientists

4,800
Open access books available

122,000
International authors and editors

135M
Downloads

Our authors are among the

154
Countries delivered to

TOP 1%
most cited scientists

12.2%
Contributors from top 500 universities

WEB OF SCIENCE™

Selection of our books indexed in the Book Citation Index in Web of Science™ Core Collection (BKCI)

Interested in publishing with us?
Contact book.department@intechopen.com

Numbers displayed above are based on latest data collected.
For more information visit www.intechopen.com

Chapter 12

Silicon Photonic Crystals Towards Optical Integration

Zhi-Yuan Li, Chen Wang and Lin Gan

Additional information is available at the end of the chapter

http://dx.doi.org/10.5772/55041

1. Introduction

During the past two decades, there have been great interests in developing ways to manipulate photons at nanoscale, realizing optical integrations, developing smaller, faster, and more efficient optoelectronic devices for the purpose of next-generation optoelectronic technology. Great progresses have been made in exploring photonic crystals (PCs) [1,2], plasmonic structures [3,4], and other nanophotonic devices for applications. However, plasmonic structures always involve some metal cells and are subject to strong energy dissipation and absorption loss in optical frequencies. Since silicon has a large refraction index and low loss in the infrared wavelength, it becomes an important optical material that has been widely used for integrated photonics applications. Meanwhile, silicon dominates microelectronics and this makes the silicon-based optical devices have the advantage to integrate with electronic devices.

Among all the semiconductor-based optical devices, a class of integrated optical devices that are built in the platform of periodically patterned silicon structures (namely, silicon PCs) are now attracting much attention [5–7]. Analogous to real crystal, electromagnetic (EM) wave is strongly modulated in PC by means of periodic Bragg scattering. Photonic band gaps (PBGs), which can prevent light from propagation in certain direction for a certain range of wavelengths, are formed similarly to electron band gaps. If we introduce a line defect or a point defect in PC, a defect state will take place within the PBG, where light is strongly localized around the defect. These defects can serve as a high efficient waveguide channel or as a microcavity with a high-quality (high-Q) factor. The mismatch of the PBGs spatial inversion symmetry breaking and could lead to the optical isolation in any device where the forward and backward transmissivity of light is very much different.In addition, the transmission bands also provide remarkable dispersion properties due to strong Bragg scattering, and negative refraction, self-collimation, superprism and many other anomalous transport behaviors [8–13] can be achieved by engineering the unit cell geometry of PCs. In this review,

INTECH
open science | open minds

© 2013 Li et al.; licensee InTech. This is an open access article distributed under the terms of the Creative Commons Attribution License (http://creativecommons.org/licenses/by/3.0), which permits unrestricted use, distribution, and reproduction in any medium, provided the original work is properly cited.

we briefly introduce the theoretical background of the light propagation in PC and show our recent results on design, fabrication, and characterization of several basic integrated optical devices in the platform of infrared silicon PC slab.

2. Theoretical and numerical tools

In this section, we briefly introduce the theoretical background and the numerical methods for our study of PC. The propagation of electromagnetic waves in PC is governed by the Maxwell equations [14]. For the sake of simplicity, we only consider a nonmagnetic linear system. In particular, the dielectric constant ε is independent of frequency and we neglect any absorption of electromagnetic waves by the material. Furthermore, there are no free charges or currents in our system. With all of the assumptions, the magnetic field within the PC satisfies the following equation that directly originates from the Maxwell equations [15]:

$$\nabla \times \left\{ \frac{1}{\varepsilon(\mathbf{r})} \nabla \times \mathbf{H}(\mathbf{r}) \right\} = \frac{\omega^2}{c^2} \mathbf{H}(\mathbf{r}). \tag{1}$$

Since our system involves a periodic dielectric function ε, we can apply Bloch-Floquet theorem to our situation, which means that the solutions can be expressed as:

$$\boldsymbol{H}_{\boldsymbol{k}}(\boldsymbol{r}) = \boldsymbol{u}_{\boldsymbol{k}}(\boldsymbol{r}) \mathrm{e}^{\mathrm{i}(\mathbf{k}\cdot\mathbf{r}-\omega t)}, \tag{2}$$

where k is the Bloch wave vector and $\boldsymbol{u}_{\boldsymbol{k}}(\boldsymbol{r})$ is a periodic function of position. This type of solutions are periodic as a function of k.

Several theoretical methods have been developed to handle different problems for PC structures, such as the plane-wave expansion method (PWEM) [15–18], transfer matrix method (TMM) [19], finite-difference time-domain (FDTD) method [20,21], and multiple scattering method [22,23]. Each method exhibits its own benefits and drawbacks. The PWEM is the earliest method applied to PC [15], and has shown its great power in the discovery of three-dimensional (3D) diamond-lattice PCs that have a complete PBG [15]. However, this method has a severe limitation in that it can only deal with the photonic band structures. The TMM is an efficient approach that was designed particularly to calculate the transmission spectra of PC, but it can also be used to solve the photonic band structures. This approach works based on the finite-difference scheme in the real space [19]. Later on, a plane-wave based transfer-matrix method (PWTMM) was developed by Li et al. [24–26]. This method works on the plane-wave space and uses plane wave functions (representing Bragg waves) to describe both the EM fields and dielectric functions. This approach can handle a broad range of general PC problems. In addition to the regular solutions of photonic band structures and transmission/reflection/absorption spectra, this approach can efficiently solve the Bloch wave scattering at

the interface between semi-infinite PC structures, because it can also work in the Bloch mode space [27]. So far, other methods have not developed such a peculiar capability. For this reason, it can calculate efficiently modal coupling with multimode PC waveguides [28], transmission efficiency through general two-dimensional (2D) and 3D waveguide bends [29], and band diagrams and field profiles of PC surface states [30]. On the other hand, this method has adopted advanced numerical and mathematical analysis tools to enhance numerical convergence and accuracy, and it has shown its superior power in dealing with some metal PC structures compared with other methods [31]. Recently, this method was also extended to solve nonlinear optical problems in ferroelectric PC structures [32,33]. The FDTD method is a very popular and universal approach in numerical simulations of various PC problems. In addition to the regular band structures and optical spectra calculations, this technique can govern the EM field evolution with time in arbitrary PC structures with infinite or finite structural domain. The reason is that the technique works in the time domain and directly solves the Maxwell equations.

Many free software packages and commercial software packages have been developed worldwide and they are widely used in numerical simulations and solutions of different PC problems. Our group has also developed homemade codes based on several methods including the PWEM, PWTMM, FDTD, and multiple scattering method. In addition, we also utilize publicly available free software packages as they are more numerically economic or have better numerical efficiency. In our case, we use MIT Photonic-Bands (MPB) package [16] to compute the photonic band structures and use MEEP, a free FDTD simulation software package developed at MIT [34] to calculate transmission spectra and model electromagnetic wave transport features in the 2D PC structures and devices.

3. Sample fabrication and optical characterization

After the discovery of PC, many novel devices have been proposed to control light and implement specific functionality of information processing. 2D air-bridged silicon PC slab [Fig. 1(a)] is an excellent platform to fabricate PC integrated optical devices. This system involves a silicon membrane suspended in air, which confines light by high index contrast in the vertical direction, while the periodic structures in the slab give a strong in-plane confinement of light through PBGs. In most cases, a typical PC structure is a kind of periodic array of air holes etched in a silicon-on-insulator (SOI) wafer by microfabrication techniques. The SOI wafer has a $Si/SiO_2/Si$ structure. In our case, it has a 220 nm thick silicon top layer and a 3 μm buried silica layer on top of a 0.5 mm thick single crystal silicon wafer. We directly use focused ion beam (FIB) lithography to drill air holes in the silicon membrane or use electron-beam lithography (EBL) to define PC patterns in a thin film of polymethylmethacrylate (PMMA), and then transfer the patterns into the silicon membrane by inductively coupled plasma (ICP) etching under the atmosphere of SF_6 and C_4F_8 gases. Figures 1(b) and (c) are the top-view scanning electron microscope (SEM) picture of our PC structures fabricated by FIB. By utilizing state-of-the-art microfabrication techniques, the optical properties of the periodic array of air holes can be easily and accurately controlled. For instance, one can change the diameters of

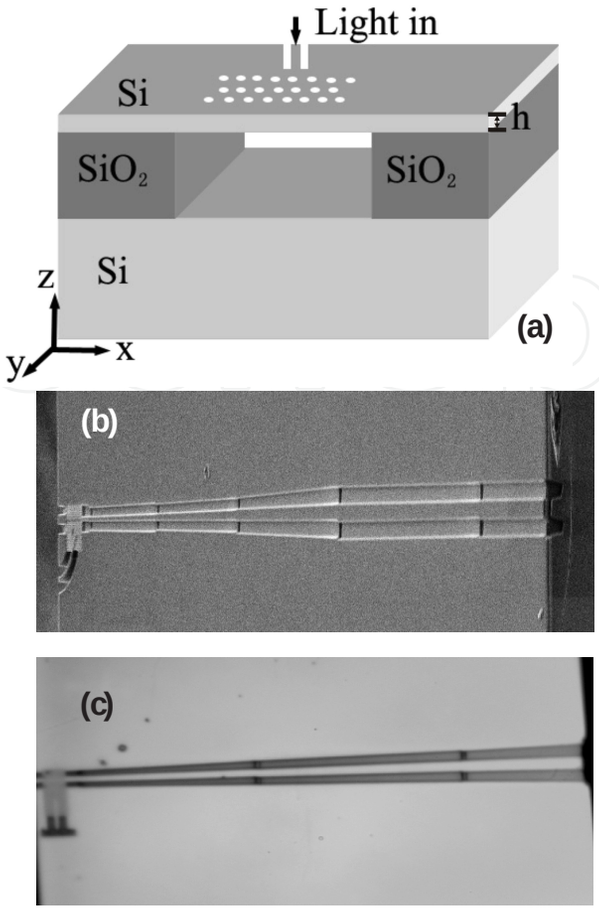

Figure 1. a) Schematic view of a 2D air-bridged PC structures with an input silicon waveguide. The whole structures are fabricated in SOI wafer. The air-bridged structures are formed by HF wet etching; (b) and (c) are the top-view SEM and optical microscopy image of a practical PC sample used in experiment. The long adiabatically tapering ridge waveguide connected with the PC structure can be clearly visualized.

certain holes or omit to etch one or several holes at certain places. These procedures can allow for engineering of the linear and point defect characteristics. After the air holes PC structures get done, we use HF acid wet etching to remove the buried oxide layer under the silicon membrane PC structures to form air-bridged structures. Usually, wide silicon wire waveguides (also with the air-bridged geometry) close to the interface of PC structures are used as the input and output infrared light beam channels, as shown in Fig. 1. These wire waveguides are further connected with long adiabatically tapering ridge silicon waveguides (each about 0.2 mm long) to allow easy coupling with external infrared signals from single mode optical fibers. As a result, a typical PC sample has a total length of about 0.5 mm and the input and output ends are carefully polished to enhance the coupling efficiency of input and output infrared signals.

The transmission spectra of a PC structure effectively reflect its optical properties. To get this important physical quantity, we have set up an experimental apparatus that involves several functional components. The overall measurement setup is schematically illustrated in Fig. 2(a), while a picture of the corresponding real system is displayed in Fig. 2(b). As shown in

Fig. 2(a), the PC samples are placed in the center of the stage, with its two sides connected with the input and output optical fibers. The input optical signal comes from a continuous wave tunable semiconductor laser with the wavelength ranging from 1500 to 1640 nm, launched into one facet of the ridge waveguide via a single-mode lensed fiber. Power meter is used to detect the optical signals transmitted through the PC structures and emitted from the output side. The measurement is made with TE polarization (electric field parallel to the slab plane) since it has a complete band gap in silicon PC slabs. The measurement data are normalized by a ridge waveguide on silicon with the same length and width to yield the final transmission spectra for a specific PC structure.

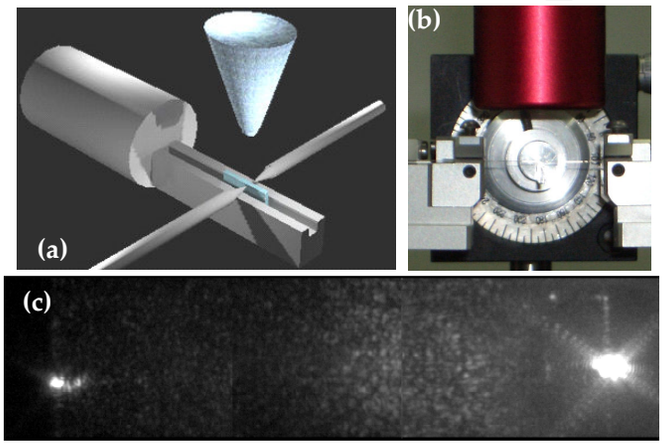

Figure 2. a) Schematic view and (b) experimental setup for the optical characterization of infrared 2D silicon PC slab structures; (c) typical optical microscopy picture recorded by the CCD camera for the PC sample as displayed in Fig. 1(b).

In addition to the measurement of transmission spectra, our experimental setup can offer another big power: it allows for easy and convenient direct monitoring of the transport path of infrared light through PC devices. As depicted in Fig. 2(a), a charge-coupled device (CCD) camera is mounted above the sample and it can *in situ* monitors the transport property by imaging the roughness induced scattering infrared light from the surface of the PC structures. The long-focus microscope objective connected with the CCD camera is shown in the upper part of Fig. 2(b). The ray trace can be directly visualized by the camera to yield images at a personal computer monitor, and this gives the researcher a rough but direct estimate abouthow much the infrared signal has gone into the PC structures. The idea is simple: if the infrared light is coupled into the PC sample with a sufficiently high efficiency, infrared light can transport along the input ridge waveguide, PC devices, and the output ridge waveguide. Significant scattering of infrared signal off the sample can take place and is collected by the CCD camera and visualized *in situ* by the monitor. The strongest scattering occurs at the discontinuity interface, including the end facets of input and output ridge waveguides and the connection section between ridge waveguides and PC structures. Even within the PC structures, remarkable scattering still takes place because of the inevitable roughness on the surface of silicon slab and within the inner walls of air holes. On the other hand, if the infrared signal coupled into the PC samples is weak, then the overall scattering light that can be collected by

the CCD camera is also very weak, and no picture can be visualized in the monitor. Figure 2(c) shows a typical microscopy picture recorded by the CCD camera. Such an experimental setup is very convenient to adjust the precise position of the input and output optical fibers, so that they have a precise point-to-point alignment with about 250 nm thick PC samples to allow for high-efficiency optical coupling. The infrared signal transporting through the PC samples usually has a power level of micro-walt when the input signal from semiconductor laser is on the power level of milli-walt. The signal has been already sufficiently strong to allow for transmission spectrum measurement and CCD camera monitoring with high signal-to-noise ratio.

4. PC band–gap devices: waveguides and cavities

4.1. PC waveguides

PC waveguides are one of the most important elements in PC integrated optics, because they offer efficient channels for light propagating at wavelength scale and connect different devices in integrated optical circuits. Usually, PC waveguides are formed by removing one row of holes in a PC structure. The line defects can generate defect states within the complete PBG and serve as waveguide channels for light to propagate efficiently and freely in PC structures. Among many 2D PC slab structures, the triangular lattice of air holes has a relatively large band gap for TE-like electromagnetic modes, where the magnetic field points in the perpendicular direction while the electric field is dominantly within the lateral plane of the slab. In addition, the structures allow for easy fabrication by standard planar nanofabrication technologies such as FIB and EBL, and have good mechanical stability. For these reasons, they are widely and dominantly adopted in designing and exploring PC based integrated optical devices [35,36].

Figure 3(a) shows the calculated TE-like mode photonic band structures of a particular 2D triangular lattice PC slab, where a wide complete PBG is clearly seen. In the region, light propagation inside the PC is prohibited. When removing one or several rows of air holes in the PC structures, some allowed modes (defect states) appear within the PBG [Fig. 3(b)], and they can be used to create waveguides or cavities. In most works, single-mode or multi-mode optical waveguides are usually made along the Γ−K direction in the triangular lattice PC. It has been well established in plenty of literatures that the number of waveguide modes as well as the width of the transmission windows can be controlled by tuning the core width of the line defects. However, waveguides along other directions in the triangular lattice PC were rarely discussed. Just like the Γ−K direction, waveguides along the Γ−M direction should also be able to guide confined modes due to the existence of a complete PBG in the 2D triangular lattice PC. By removing a line of diamond areas, we can obtain a cluster-like waveguide along the Γ−M direction as depicted in Fig. 4(a). This kind of waveguide is called Γ−M waveguide [37].

Figure 4(b) is the SEM picture of the original Γ−M waveguide, where the air holes remain to locate at the original lattice site and the radius of all air holes remains the same. The air holes

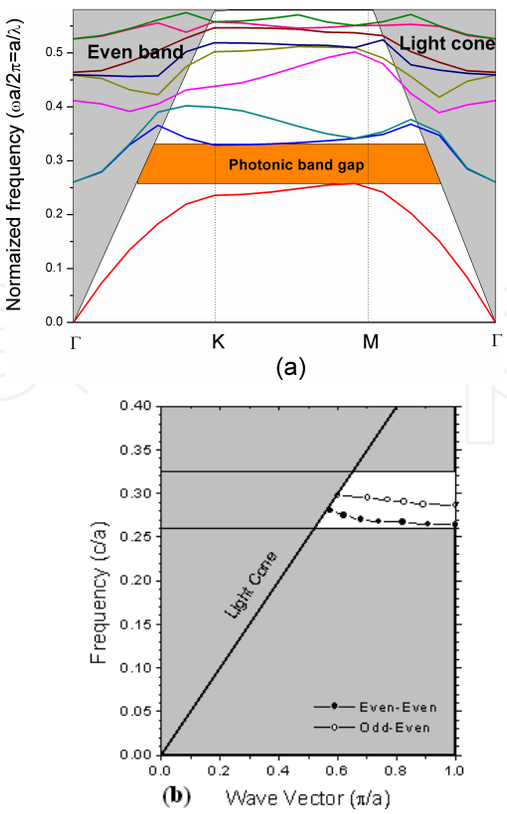

Figure 3. a) Photonic band structures for air holes triangular lattice PC slab; (b) band diagrams for a PC W1 waveguide, where one row of air holes is removed along the Γ–K direction. The upper and lower bands correspond to the even-symmetric and odd-symmetric guided mode, respectively.

are directly drilled by FIB and the lattice constant is 430 nm. According to our simulation and experiment results, we find that the width of the propagation modes for the original Γ–M waveguide [Fig. 4(b)] is only 22 nm. Then we optimize the geometry to improve its transmission characteristics. We shrink the radius r_1 of the air holes in the two nearest-neighboring rows around the waveguide and enlarge the radius r_2 of the air holes in the two second-nearest-neighboring rows, as shown in Fig. 4(c). The key point is to generate a transport pathway with walls as smooth as possible. According to our simulations, the parameters corresponding to an optimized waveguide are that r_1 = 50 nm and r_2 = 170 nm, while the radius of the original air holes is r_0 = 120 nm. Figures 5(a) and (b) are the calculated dispersion relations of the original and optimized Γ–M waveguide, respectively. It's shown that the optimized waveguides have a high pass band that is much broader than the original waveguide. We can also obtain the same conclusion from the measured transmission spectra in Figs. 5(c) and (d). Besides, the intensities of the transmission spectra are much higher than the original one. As the Γ–M waveguide is perpendicular to the usual Γ–K waveguide, it offers an alternative to construct a waveguide interconnection beyond the usual scheme of Γ–K with Γ–K waveguides. A high-performance wide-band Γ–M waveguide should be of great help to build integrated-optical devices, such as interconnection networks, channel-drop filters, and wave division multiplexers, with more flexible geometrical configurations in 2D PC slabs.

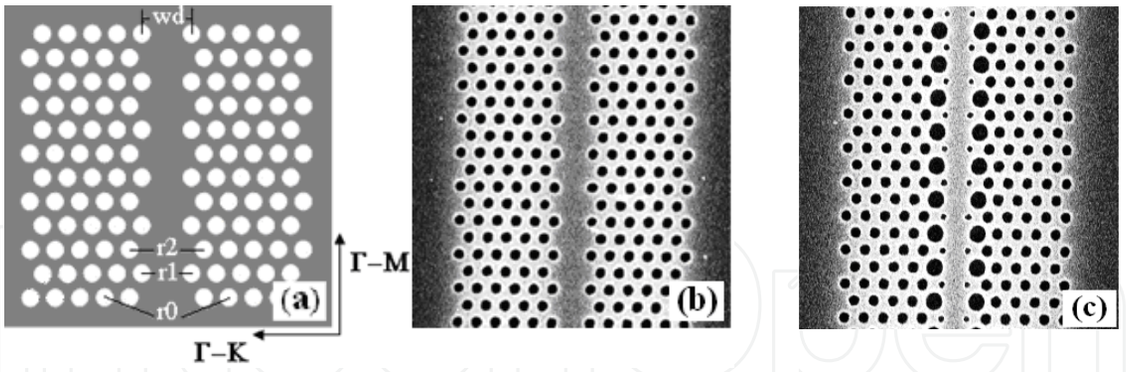

Figure 4. a) Schematic of Γ–M waveguide constructed in a triangular-lattice PC slab. The width of the waveguide w_d, as well as the radius of air holes in the first and second row r_1 and r_2, are the three crucial parameters to optimize the width of the transmission windows; (b) and (c) are SEM pictures of original and optimized Γ–M waveguides [37].

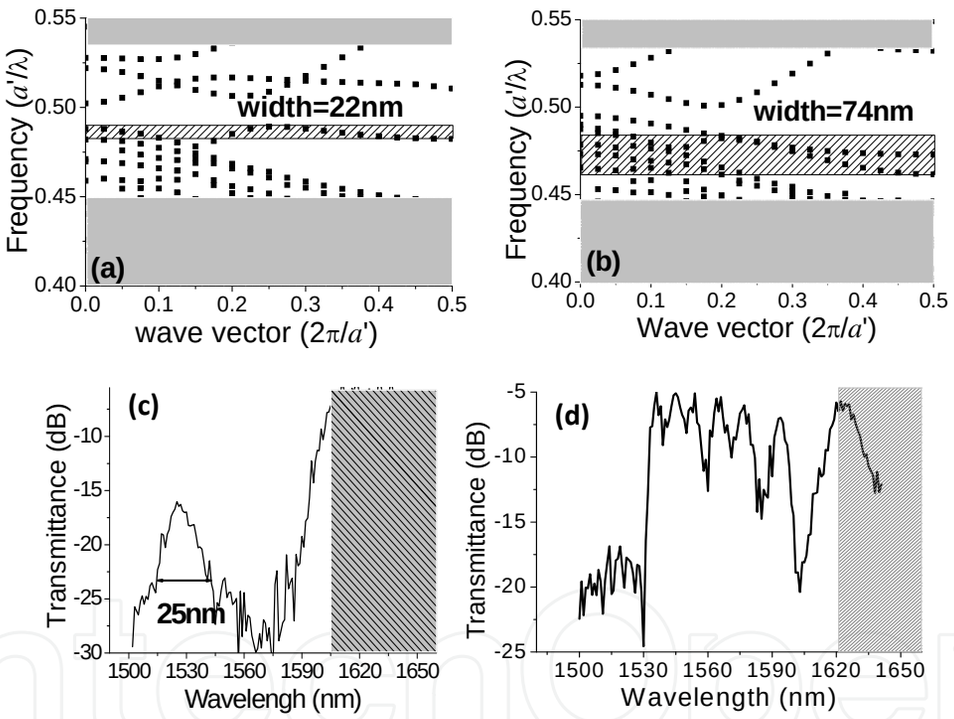

Figure 5. Calculated modal dispersion relation of (a) the original Γ–M waveguide and (b) an optimized Γ–M waveguide. The band width of the waveguide modes (within the dashed boxes) is 22 nm in the original waveguide, which has parameters: lattice constant a = 430 nm, hole radius $r_0 = r_1 = r_2 = 120$ nm, and waveguide width $w_0 = 2a$. After optimization by the following parameters as a = 430 nm, r_1 = 50 nm, r_2 = 170 nm, and $w_d = 0.65w_0$, the waveguide band width is significantly broadened to 74 nm; (c) and (d) are the corresponding measured transmission spectra of the original and optimized waveguides [37].

Based on the design of an optimized Γ–M waveguide, we combine the Γ–K waveguide and Γ–M waveguide together to form a 90° waveguide bend as schematically depicted in Fig. 6(a) [38]. This is the first design of a 90° waveguide bend in the 2D triangular-lattice PC. The whole waveguide bend system is composed of two Γ–K waveguides as the input and output ports

and the center Γ−M waveguide as the connection component. In other words, the structure involves two consecutive segments of 90° waveguide bends. In constructing the waveguide bend, we have used the optimized Γ−M waveguide discussed in the above and depicted in Fig. 4(c). The guided modes in the optimized Γ−M waveguide have better phase-matching and mode profile matching with the normal Γ−K waveguides. In the same time, we modify the bend corner geometry by fabricating smaller air holes in the corner to make the guided modes between the two kinds of waveguides matching better. Based on a serial of simulation and experiment tests, we find the best values for r_1 and r_2. Figure 6(b) shows the SEM picture of the waveguide bend with r_1 = 50 nm and r_2 = 150 nm. After optimization, we get 70 nm pass band width while the transmission efficiency of a single bend is 45%. The proposed 90° waveguide bends can help to construct integrated optical circuits with more flexible and diversified infrastructures.

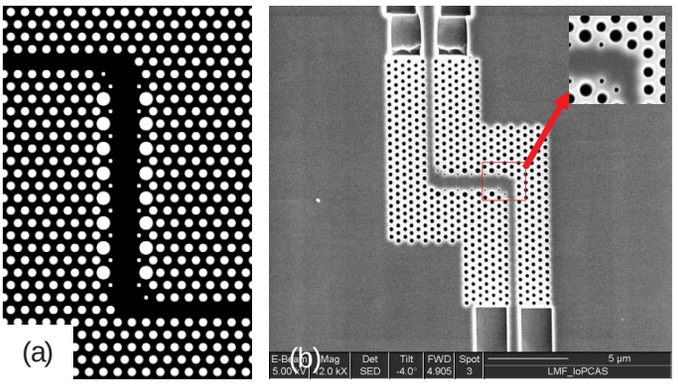

Figure 6. a) Schematic geometry of 90° waveguide bends in a triangular lattice PC slab with optimized Γ–M waveguide; (b) SEM picture of a practical sample of 90° waveguide bends with optimized bend corner geometry [38].

4.2. Coupled–cavity waveguide

Moreover, we have designed an air-bridged silicon PC coupled-cavity waveguides (PCCCWs) [39] and mapped its near-field optical distributions at different wavelengths around 1550 nm with the scanning near-field optical microscopy (SNOM) technology. For PCCCWs, the eigenmodes usually have relatively narrow bandwidth with slow group velocity in the whole band range. Previously, slow light propagation in such specific PCCCWs had still not been experimentally studied via SNOM technique. Figures 7(b)–7(f) show the calculated optical field distribution profiles at different wavelengths with a simulation model schematized in Fig. 7(a). We fabricated the PCCCW in the SOI wafers with FIB system. Figure 8(a) displays the SEM image of the element composed of the central PCCCW (encircled by a red square), two identical W1 PC waveguides, and the input/output ridge waveguides. Figure 8(b)–8(f) displays the near-field optical intensity distribution patterns of the PCCCW at different wavelengths. The scanning area is 12 μm × 15 μm with the incident light propagating upwards from the bottom of the image. Straight yellow lines in Figs. 8(b)–8(f) are used to label the position for showing the cross-sectional profiles of the field distribution patterns.

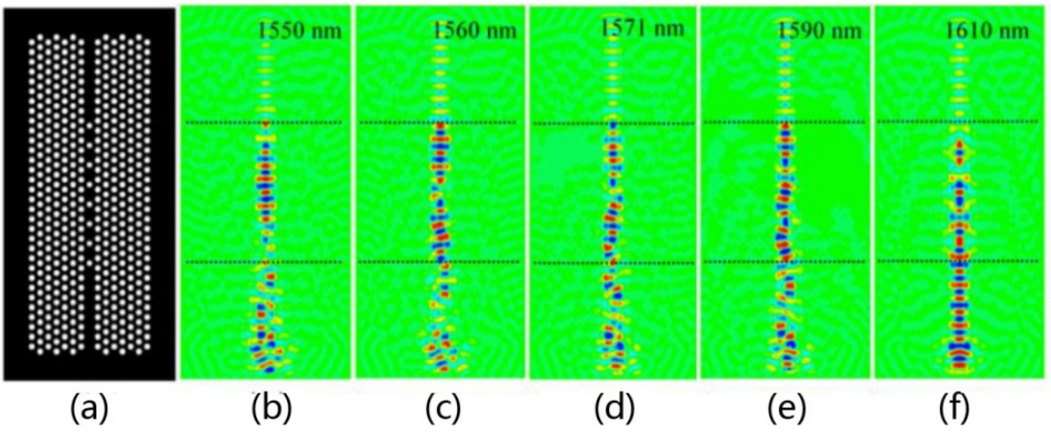

Figure 7. Simulation model (a) and calculated optical field distributions at (b) 1550 nm; (c) 1560 nm; (d) 1571 nm; (e) 1590 nm; and (f) 1610 nm [39].

The optical intensity distribution patterns are different at 1550 and 1610 nm, even though both of them mainly appear as a single narrow line along the central PCCCW region with a full width at half maximum (FWHM) of about 350 nm. Precisely speaking, the pattern demonstrates a little bit shoulder as a result of mode superposition at 1550 nm, since it comprises two eigenmodes. At 1610 nm, the calculated result consists well with the experimental one in Fig. 8(f), which presents a single line along the whole waveguide. The pattern appears bright and wide with obvious interference nodes in the PCCCW section. The simulated field distribution profiles in the W1 PC waveguide sections agree well with the detected ones at all these wavelengths, which show a snake-like/single-line profile in the input/output W1 PC waveguide except that of a snake-like profile in the output W1 PC waveguide at 1560 nm. In addition, the simulated field distribution patterns of the snake-like profile in the PCCCW section appear deviating greatly from the detected ones at 1550, 1571, and 1590 nm. However, if we calculate the optical field distribution patterns at 1550, 1560, and 1571 nm with the even-to-odd amplitude ratios of 1:4, 1:1, 1:4, and 1:6, respectively, we can find the simulated results are consistent with the experimental patterns evolving from single-line, to snake-like, and then to double-line structures for the PCCCW section. Combination of the near-field optical detection and theoretical simulation shows that SNOM is an efficient tool to study the optical propagation in the PCCCW and can help to design slow light elements.

4.3. High–*Q* cavity

Quantum information processing and quantum state manipulation have received great attentions because of their potential revolutionary impact on future network communication. Optical cavities, which can be used to store information, are considered to be one of the most important devices in the quantum communication application. The generation and teleportation of qubits require sufficiently high value of Q/V, where V stands for the mode volume of the optical cavities. As a result, high-Q optical cavities show great potential application in quantum information. Among all the optical cavities, 2D PC slab cavities are the best choice because of their simultaneous high-Q and small mode volume characteristics. It has been

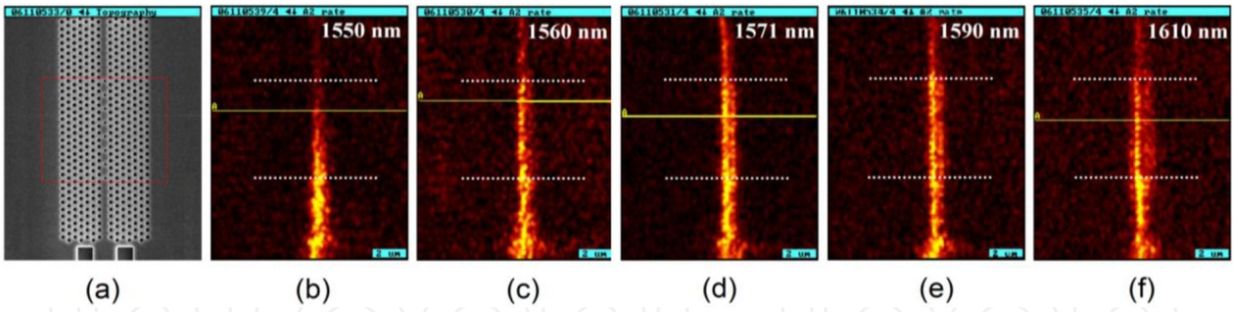

Figure 8. a) SEM topographic image, and the near-field optical intensity distributions at (b) 1550 nm; (c) 1560 nm; (d) 1571 nm; (e) 1590 nm; and (f) 1610 nm. The white dotted lines in each optical picture denote the interface between the W1 PC waveguide and PCCCW. All pictures were obtained for the same scanning area of 12 μm × 15 μm [39].

reported that Rabi splitting can be observed experimentally when the quantum dots are introduced into the PC cavities with high Q/V [40,41]. Moreover, due to the development of nanofabrication technique, multiple high-Q PC slab cavities can be fabricated at the same time on a single slab by the EBL and ICP etching technique. Once atoms or quantum dots are embedded into the high-Q PC cavities, various quantum phenomena can be demonstrated on chip. Recently, our works on high-Q silicon PC microcavities have achieved great progress after extensive exploration and delicate improvement of nanofabrication techniques and sample processing techniques have been made [42].

We focus on studying the L3 PC microcavities formed by removing three cylindrical air holes in the Γ−K direction in a triangular lattice [Fig. 9(a)]. The lattice constant is 430 nm, the radius of cylindrical air hole is 120 nm and the thickness of silicon slab is 235 nm. The FDTD calculation results indicate that the L3 PC microcavity possesses a quality factor of about 5300 [Fig. 9(c)]. After trying hundreds of simulations, we find that the positions of air holes at the edges of the microcavities affect the Q factor dramatically. The electric field pattern of the cavity mode can be tuned to be Gaussian-type by displacing the six air holes outwardly at the edges of the microcavities, and this can increase the quality factor significantly [41,42]. The optimal displacement is found to be 73, 10 and 73 nm for the first, second and third air holes at both edges of the microcavities, which is depicted in Fig. 9(b). The maximum quality factor of 127,323 [Fig. 9(d)] can be achieved, which is 20 times larger compared with the unadjusted one.

Based on the optimal parameters, we successfully fabricate the designed high-Q planar L3 PC microcavities in SOI wafer by implementing EBL and ICP [42]. As can be seen in Fig. 10(a), the L3 microcavity is side-coupled to a W1 waveguide with the barrier of three rows of air holes. The samples are measured by our home-made fiber coupling system as described in the above section. When the incident wavelength is off-resonant, light cannot couple with the microcavity, leading to strong output. While, at resonance most energy is tunneled into the microcavity, resulting in weak output. For the case of high-Q microcavity, a sharp transmission dip is expected in the transmission spectrum. The lattice constant, radius of cylindrical air hole and the thickness of silicon slab are 430, 120 and 235 nm, respectively. Limited by the fabrication accuracy of 10 nm, the displacement is adjusted to be 80, 20 and 80 nm for the six air holes at both edges of the microcavities. Figure 10(a) shows the enlarged

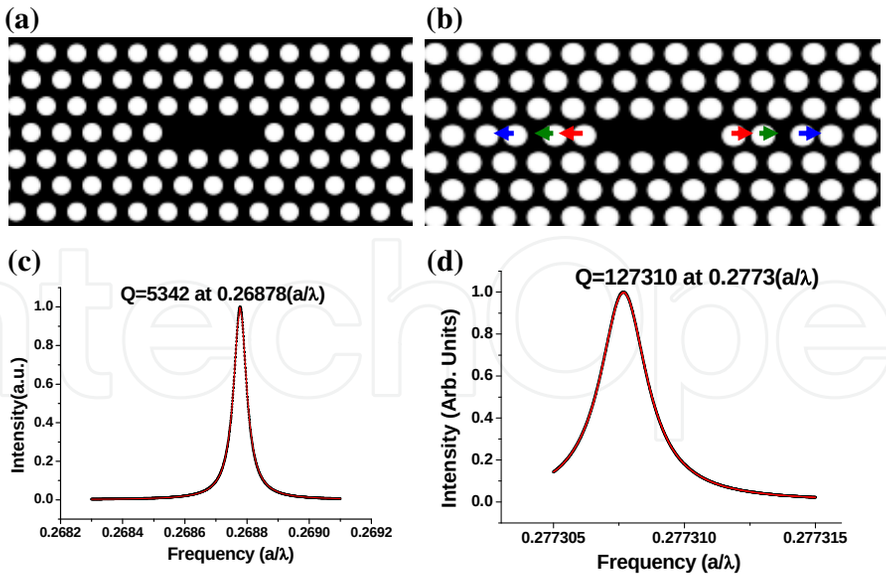

Figure 9. Schematics of (a) the original PC L3 nanocavity and (b) the optimized nanocavity; (c), (d) show radiation spectra of the original PC L3 nanocavity and the optimized nanocavity, respectively [42].

view of the cavity region. A sharp and narrow transmission dip is observed at the 1567.35 nm in the measured transmission spectrum [Fig. 10(c)]. For the purpose of extracting the quality factor accurately, we finely tune the wavelength between 1565 and 1570 nm. The measured spectrum is illustrated in Fig. 10(d) and the *Q*-factor as large as 71,243 is obtained. Nevertheless, there are some deviation between the simulation and experiment. For example, the resonant wavelength is 16.75 nm red-shifted from the simulated result and the maximum quality factor is significantly less than the calculated value of 127,323 [Fig. 10(b)]. We believe that the deviation is caused by the imperfection of the cylindrical air holes and the actual radius is not exactly the same as the value in simulation. The success of fabricating high-*Q* silicon PC slab microcavities enables us to investigate various interesting quantum phenomena, such as strong coupling between light and quantum system, quantum information processing technique, single photon source, all-solid quantum manipulation and high-quality biochemistry sensing devices.

4.4. Channel drop filters

Channel drop filters are key components for extraction of light trapped in a point-defect cavity to a neighboring waveguide and they sit on the basis of wave-division multiplexers and demultiplexers. They have great applications in a wide variety of fields, such as photonic integrated circuits, telecommunications, and quantum informatics. Based on the simulation and experiment experiences about PC waveguides, we design and fabricate an ultra compact three ports filter in 2D air-bridged silicon PC slab by closing the bus waveguide for 100% reflection feedback. Figure 11(a) shows the SEM picture of the three ports filter structure [43]. This filter was fabricated by EBL and ICP techniques. The lattice constant of the PC and the radius of the air hole are 430 and 145 nm, respectively. Port 3 is the input waveguide channel, while ports 1 and 2 are two output waveguide channels, respectively. They are formed by

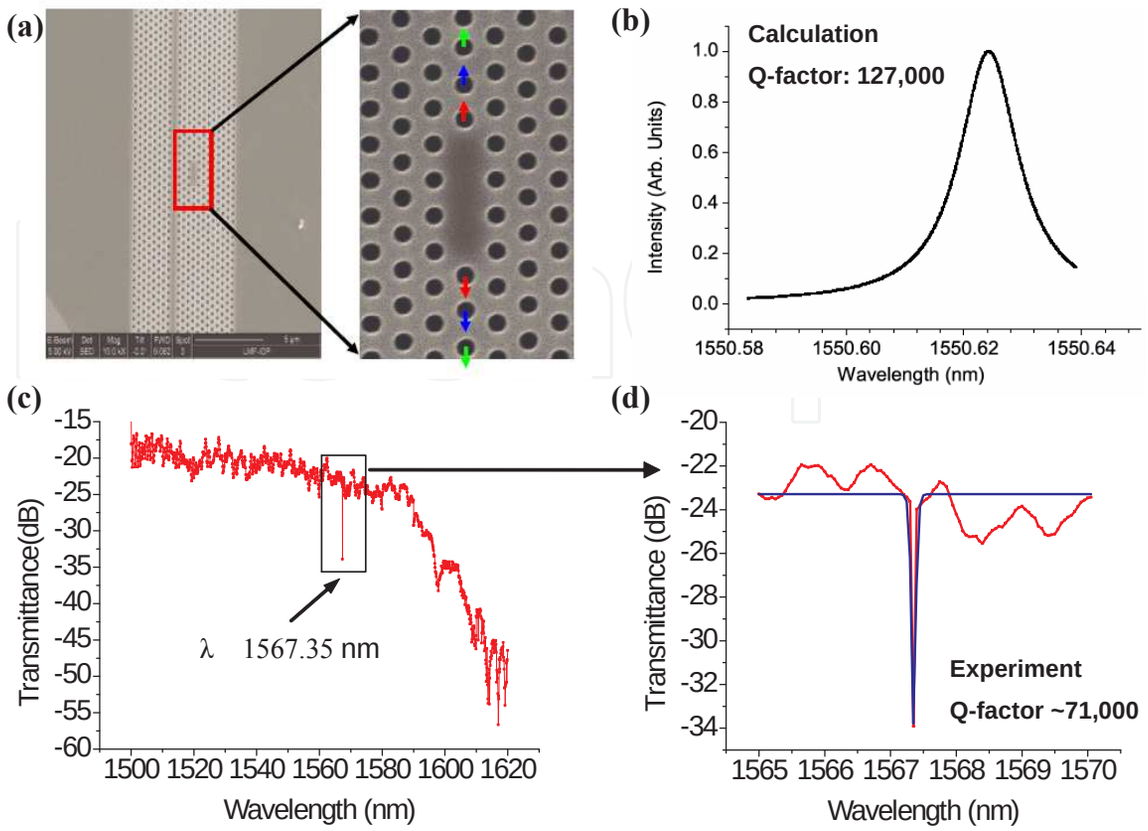

Figure 10. a) SEM pictures of one of the fabricated samples, including the L3 nanocavtiy with displaced air holes; (b) radiation spectra calculated by FDTD method; (c) and (d) show transmission spectra of one of the fabricated samples. The maximum *Q* value of up to 71000 is obtained [42].

missing one row of air holes along the Γ−K direction of the triangular-lattice PC, the so called W1 waveguide. C1 and C2 are two point-defect cavities. The distance between the center of the defect cavity and the neighboring waveguide is 3 rows of holes in the *y* direction. As seen in Fig. 11(a), the C1 cavity consists of three missing air holes, and the two air holes at the cavity edges are shifted outward by 10 nm apart from the regular positions. Similarly, those of the C2 cavity are shifted by 20 nm. The slight shift of air holes is conducive to confine light inside the cavity and leads to a higher quality factor. Meanwhile, the different shifts of the two cavities make the resonant wavelengths slightly different. The experiment results [Figs. 11(b) and (c)] show that the resonant wavelengths of C1 and C2 are 1529.5 and 1531 nm, respectively. The wavelength spacing of the two cavities is about 1.5 nm and might be further reduced by continuously changing the size of the cavity. The full widths at half maximum of the peaks are 1.5 and 1.4 nm and the corresponding quality factors are about 1020 and 1090, respectively. To estimate the drop efficiency, a reference straight waveguide of the same parameters is positioned near the three-port filter. By keeping the same intensity of input light, the transmission intensities of the reference waveguide and port 1 are 0.330 and 0.158 μw, respectively, when the input wavelength is set at 1529.5 nm. The drop efficiency of port 1 is roughly estimated to be 48% and a similar result has been obtained at port 2.

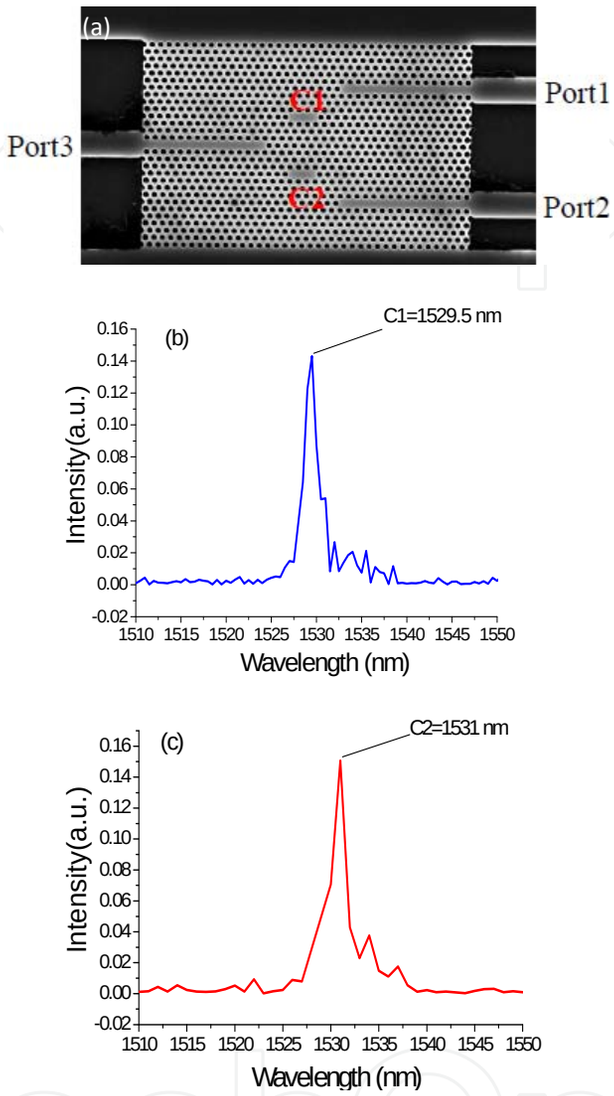

Figure 11. a) SEM image of the three-port filter; (b) and (c) the measured transmission spectra at ports 1 and 2, respectively [43].

It has been well known that structure is the kernel of filter design. Usually, the regulation of microcavity resonant frequency is obtained by changing the size of the cavities. We have proposed a new way to design multi-channel filters by changing the shape of the air holes [44]. When the shape of the air holes changes from circle to ellipse, two parameters, the ellipticity and the orientation angle of the ellipse, in addition to its size can be further explored and they can have a great influence on localized cavity modes. Therefore, we can use this for some special purpose.

Figure 12(a) schematically shows a one-channel PC filter. A horizontal channel (W1 waveguide) serves as the input signal channel, which is created by removing a single line of air holes along the Γ−K direction. A cavity is formed by removing three air holes along the Γ−K direction that is rotated 60° from the W1 waveguide. It is located four rows away from the major channel and is connected with the major channel through an indirect side coupling. Another single-mode waveguide is formed parallel to the cavity and serves as the output signal channel. Figure 12(b) shows an enlarged picture of the filter in the region around the cavity. One of its axes is oriented counterclockwise by an angle θ to the x axis, namely, the input light propagation direction. The sizes of the axes parallel and perpendicular to this orientation are a and b, respectively. Now we have great structural freedom to tune the optical properties of the new PC filter by changing the parameters of θ, a and b. To show this point, we design and fabricate a four-channel PC filter by using different cavity parameters as described in Table 1. The SEM picture of the fabricated four-channel filter is displayed in Fig. 13(a). Four cavities are located on the two sides of the central linear W1 waveguide. They are engineered by leaving several air holes unetched in the Γ−K orientation. The input signal propagates upwards from the bottom input ridge waveguide. Each cavity is coupled with another W1 waveguide that is connected to a ridge waveguide, which serves as the output signal channel.

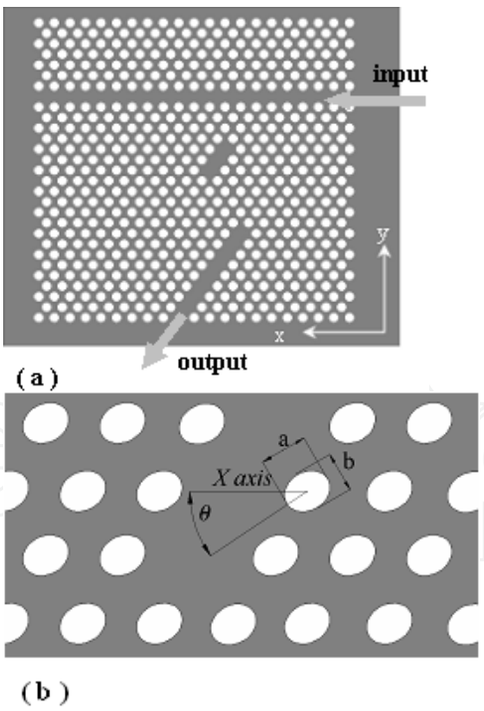

Figure 12. a) Schematic view of a one-channel PC filter, the major channel lies in the x direction, and the cavity and output side channel are parallel to the Γ−K direction of the triangular lattice; (b) enlarged view of the filter around the cavity. The air holes have a general elliptical shape with one of its axes oriented counterclockwise by an angle θ with respect to the x axis. The two axes are of size a and b, respectively [44].

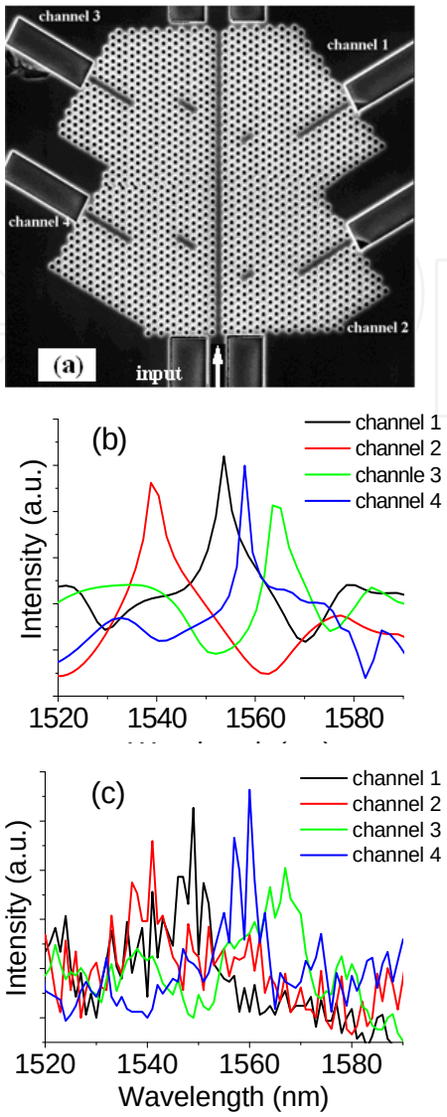

Figure 13. a) SEM image of the four-channel filter; (b) Simulation results of transmission spectra for the four-channel filter. (c) Experiment results of transmission spectra for the same filter [44].

channel	lattice constant /nm	number of missing air holes in cavities	long axis *a* /nm	shot axis *b* /nm	angle *θ*	theoretical resonant peak /nm	measured resonant peak /nm	deviation nm
1	420	2	240	200	0	1553	1549	4
2	430	2	260	240	0	1539	1541	2
3	420	3	240	220	0	1563	1567	4
4	430	3	280	240	0	1558	1560	2

Table 1. Structural parameters in the four-channel filter

The simulation and experimental results of the transmission spectra for the four channels are displayed in Figs. 13(b) and (c). Although significant noise exists, a resonant peak can be clearly found for each channel. The peaks are located at 1549, 1541, 1567, and 1560 nm for channels 1, 2, 3, and 4, respectively. The results confirm that the air-hole shape has a great influence on the functionality of the PC filter devices. The elliptical air holes can induce a fine tuning of the resonant wavelength by changing the ellipticity of the elliptical air holes.

As described in the preceding section, a high-performance wide-band Γ−M waveguide can be formed by modifying the radii of the air holes along the pathway. The combination of Γ−M waveguides and Γ−K waveguides can offer a more flexible way to interconnect and couple between different devices. We have proposed a type of PC filter using these two kinds of waveguides [45]. The Γ−M waveguide and Γ−K waveguide are used as the input and output signal channels respectively, and they are connected via cavity resonance. Figure 14(a) shows the SEM picture of a four-channel filter structure. We change the size of the cavities by moving the end points of the cavity [marked with "a, b" and "c, d" as shown in the inset of Fig. 14(b)] to change the resonant frequency. Table 2 gives the detailed parameters of the four cavities. The experiment demonstrates that the four resonant peaks are at the wavelengths of 1543, 1545, 1548 and 1551 nm, as shown in Fig. 14(b). In spite of the slight shift in the resonant peak toward higher frequency, which we believe is induced by the uncertainties in the fabrication, the experimental results are in fairly good agreement with the simulation results, where the maximum relative deviation of resonant wavelength is within 2 nm. These results clearly demonstrate that the designed Γ−M waveguides can act together with the usual Γ−K waveguide to construct high-performance multichannel filers with more structural flexibility. In our experiment, we also use the CCD camera to directly monitor the transport of infrared signal within the channel-drop filter. The situation of on-resonance and off-resonance can be clearly visualized and distinguished from the CCD camera images. One typical case is shown in Fig. 14(c).

5. PC band–engineering devices for anomalous transport control

In previous sections, we discuss several PC devices, including waveguides, cavities, and channel-drop filters that are built on the silicon 2D PC platform. These devices work on defects that are brought into PBG and they can be considered as PBG materials. As we have mentioned, PC structures possess another important feature: photonic pass bands. In this section we show several example devices that implement the dispersion and refraction properties of PCs at their transmission bands.

Let's first make an overview of how band dispersion engineering works. Figure 15(a) shows the typical photonic bands structure of an air-bridge PC slab structure composed of a square-lattice array of air holes etched in silicon slab. The areas labeled in Fig. 15(a) show the unconventional light propagation, self-collimation and negative refraction, in PC. One effective way to understand and exploit desirable light propagation properties in PC is using the equifrequency surface (EFS) contours, as shown in Figs. 15(b) and 15(c). Figure 15(b) shows the EFS contours of the first TE-like band. The EFS contours in the red line frame are flat, meaning that

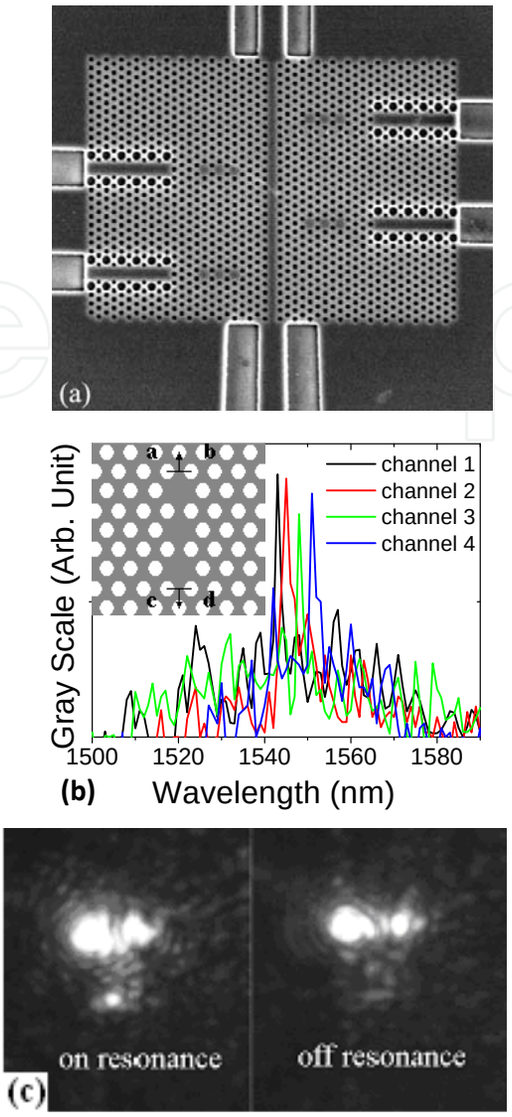

Figure 14. a) SEM image of the fabricated four-channel filter. Four cavities are located on the two sides of the input waveguide; (b) experimental transmission spectra of the four channel filter in linear scale. The inset picture illustrates two groups of end points (air-hole centers) of the cavity marked with "a, b" and "c, d." Black arrows indicate the moving direction of these air holes; (c) infrared CCD camera imaging of the output signal observed in experiment for one channel of the sample. A bright spot appears at the end of the output channel when the input wavelength coincides with the resonant wavelength and disappears when it is at off-resonance [45].

this is the self-collimation region. The reason is that the group velocity, which is parallel to the gradient of the EFS, is pointing in the same direction for all the modes located within the region. As a result, if light propagates along the Γ−M direction, it does not suffer any diffraction in the PC. $\Gamma = (0,\ 0)(\pi / a)$ and $M = (1,\ 1)(\pi / a)$ are high-symmetric points in the first Brillouin zone for square lattice. This kind of PC structures can be used as the channelless waveguide in integrated optic devices. Figure 15(c) shows EFS contours of the second band. The EFS contours are roughly circular around the direction at the reduced frequency (a / λ) range 0.28–0.31, as indicated in the red solid line frame. When the frequency increases, the EFS contours move toward the Γ point, which indicates the existence of negative refraction in the region. If the

channel	end points moving distance /nm	theoretical resonant peak /nm	measured resonant peak /nm	theoretical distance from channel 1 /nm	experimental distance from channel 1 /nm	deviation /nm
1	0	1550	1543	-	-	-
2	5	1551.5	1545	1.5	2	0.5
3	10	1553	1548	3	5	2
4	15	1556	1551	6	8	2

Table 2. Structural parameters in the four channel Γ–M and Γ–M waveguides filter

incident light is mainly parallel to the $\Gamma - M$ direction, the PC will behave like an isotropic medium with a negative index of refraction in that particular frequency range.

5.1. Negative refraction

Based on the above analysis, we designed and fabricated an air-bridged PC structure that exhibited negative refraction of infrared light [46]. The structure is schematically shown in Fig. 16(a). These structures are directly drilled by FIB technique. The input infrared signal channel is a silicon wire waveguide, which is inclined with respect to the surface normal by 10°. The lattice constant a of the square array is 460 nm and the diameter of the air hole is 220 nm. We first use 3D FDTD method to simulate the electromagnetic field intensity distribution at wavelength 1503 nm. The result is displayed in Fig. 16(b). We find strong reflection and scattering at the interface between the input waveguide and the PC structure. This is induced by the serious impedance mismatch at the interface, although the high index contrast air-bridged structure can achieve good optical confinement. To surpass this obstacle, we use a tapered air-holes connection layer at the input surface of PC structure to reduce the reflection and scattering losses. As shown in Fig. 16(b), a large fraction of light power from the input waveguide is coupled into the PC structure and negative refraction of light beam within the PC structure is clearly seen. Besides, the reflection or scattering of light at the input interface of the PC is very much reduced. This clearly indicates that the designed tapered interface can reduce the interface impedance mismatch remarkably. The calculated value of negative refraction angle is −45°.

In our measurement, TE-polarized light from a tunable semiconductor laser (1500−1640 nm) was first launched into a tapered single mode fiber, and then coupled to the silicon wire waveguide, and finally incident on the PC structure. The ordinary way to see the light propagation behavior is to directly observe the pattern of the radiated light from the top of the sample using a conventional microscopy objective and an infrared CCD camera. The result is shown in Fig. 16(c). The light spot at the middle bottom part of the pattern is the radiated light from the input silicon wire waveguide. The big light spot at the center represents the scattered light at the interface between the input wire waveguide and the PC due to impedance mismatch. There is also a small bright spot at the top right corner of the pattern, and it is

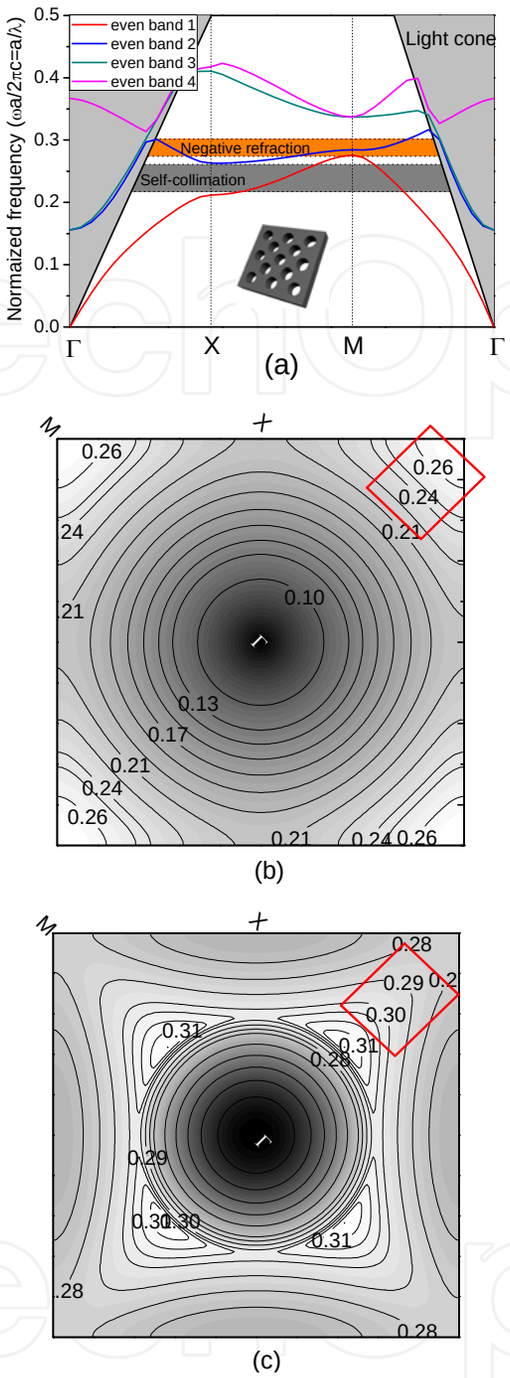

Figure 15. a) Photonic band structures of TE-like bands for an air-holes square-lattice PC slab; (b) EFS contours of the TE-like first band for the same PC show that self-collimation can occur in the direction around the Γ–M direction; (c) EFS contours of the TE-like second band show that negative refraction can occur in the direction around the Γ–M direction [46].

recognized to result from the radiated light when the negative refraction beam hits the end facet of the PC structure. Because the TE-like modes are strongly confined guided mode on the silicon slab and the surface fields are nonradiative and evanescent with respect to the vertical direction of the PC slab, the far-field pattern observed and recorded by the ordinary

optical microscopy is not able to reveal the detailed process about how the negative refraction beam propagates inside the PC structure unless the scattering of light by roughness and irregularity is sufficiently strong on the beam propagation path. This is indeed the case for Fig. 16(c). In fact, the small bright spot could not appear without the intentional introduction of the air slot at the far end of the PC structure. It would not be possible to tell which way the infrared beam would refract if without the aid of this scattering light spot.

In order to observe clearly and tell unambiguously the ray trace of the negative refraction beam in the PC structure, we used the SNOM technology (SNOM-100 Nanonics, Israel). A probe scans in the vicinity of the surface of the PC structure and records the near-field intensity distribution. The tip has a resolution of about 100 nm, i.e., 1/15 of the wavelength. The signal is recorded by an infrared single-photon detector, which allows us to capture very weak infrared signals. The probed near field information directly reflects light propagation properties of the TE-like modes for the PC and enables one to visualize the ray trace of the negative refraction light beam because the near field at the surface is an integral part of the modal profile of the confined guided modes that exponentially decay away from the surface of the slab. In the SNOM picture [Fig. 16(d)], a bright spot also appears at the front interface of the PC structure, but it is much smaller than the one in Fig. 16(c). The ray trace of the incident light beam along the silicon wire waveguide and its propagation along the negative refraction direction inside the PC structure can be clearly seen. The negative refraction angle is about −45°, which is in good agreement with the FDTD simulation presented in Fig. 16(b). The SNOM detection unambiguously discloses the negative refraction property of the designed PC.

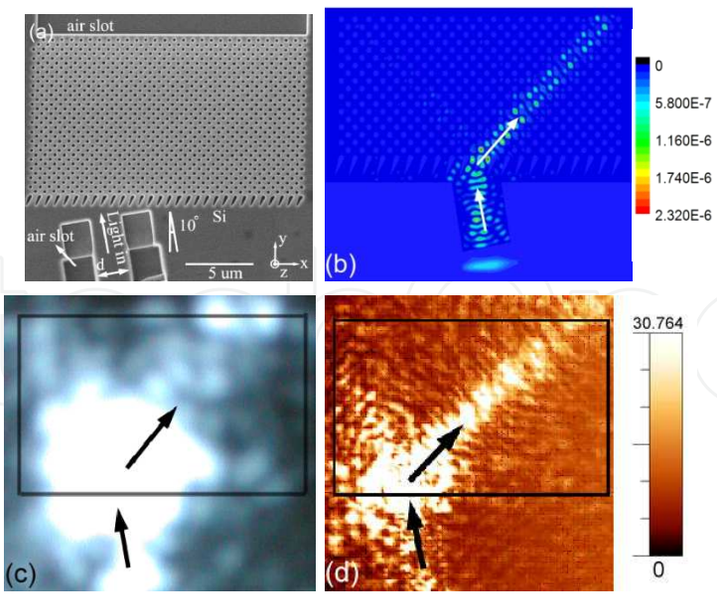

Figure 16. a) SEM picture of the PC structure and an input waveguide. The width of the waveguide *d* is 2 μm; (b) Light intensity distribution of TE-like modes for PC with deliberately designed tapered air-holes interface; (c) Directly observed pattern of the radiated light of $\lambda = 1500$ nm from the top using an objective lens; (d) SNOM picture of the negative refraction of the same wavelength. In each picture, the boundary of the PC structure is superimposed as solid lines [46].

On the other hand, ordinary positive refraction only occurs for TM-like confined modes, so the designed PC structure can behave as an efficient beam splitter in an integrated optical circuit. The high-resolution SNOM technology can greatly help one to directly visualize the ray trace and acquire deeper understanding on various anomalous wave propagation behaviors, such as super-prism, superlensing, self-collimation, and slow light in deliberately designed 2D PC slab structures in the optical wavelengths. This in turn can help to explore a wider regime of controlling light behaviors on the nanoscale for future basic science and high technology applications.

5.2. Self–collimation effect

Self-collimation effect is the propagation of light without diffraction along the propagation direction. This phenomenon has been used to construct non-channel waveguides, beam splitters and beam combiners [47,48]. The behaviors of these devices are determined by the performance of the self-collimation effect. Recently we have designed and realized a simple structure composed by a square lattice array of elliptical air-holes where broadband large-angle self-collimation effect is observed for TE-like guided modes in infrared wavelength [49].

Figure 17(a) shows our PC structure formed by a square lattice of elliptical holes. The calculated TE mode photonic band diagram of the fourth, fifth and sixth bands are shown in Fig. 17(b). The self-collimation effect can be observed at the gray regions within a broad normalized frequency range 0.36−0.39 and 0.43−0.46. For simplicity, we only consider the EFS contours of the fifth TE band [Fig. 17(c)]. The contours are flat at the normalized frequency between 0.43 and 0.46 for all the values of k_y and not just in the vicinity of $k_y = 0$. This feature indicates that our structure can support self-collimation for incident light beams with large incident angles. Then the FDTD simulation by using the MEEP package is performed to verify our prediction. A structure with the size of 30 a× 45 a is considered. A Gaussian beam with a width of 4a propagates into the surface at 0°, 20° and 60° incident angles (Fig. 18). For simplicity, we only consider the minimum (0.36) and the maximum normalized frequency (0.43). Figure 18 shows the electric field intensity distribution in the xy plane with 0°, 20° and 60° incident angles at normalized frequency 0.36 [Fig. 18(a)] and 0.46 [Fig. 18(b)]. From the simulation results, we find that the light beam is collimated along the propagation direction for each situation. However, the couple efficiency of the incident light becomes lower and lower with the increase of the incident angle. We do not show the field distributions for those incident angles that are larger than 60°. These six situations in Fig. 18 are sufficient to show the broadband large-angle characteristic of the self-collimation effect.

Following our simulation results, we fabricate our PC structures in SOI substrate by EBL and ICP etching process. Figure 19 shows the SEM pictures of the designed PC structures with 0°, 20° or 60° incident waveguides. Ray trace of light beam is observed using IR camera and a high numerical aperture (NA = 0.50) objective. Detailed images of the field intensity of the scattered light are recorded for 0°, 20° and 60° incident angles for different incident wavelengths. Here we only show the patterns of the minimum and maximum wavelengths for each incident angle. They demonstrate strong light confinement along the propagation direction for all the situations. The experimental results are in good agreement with FDTD

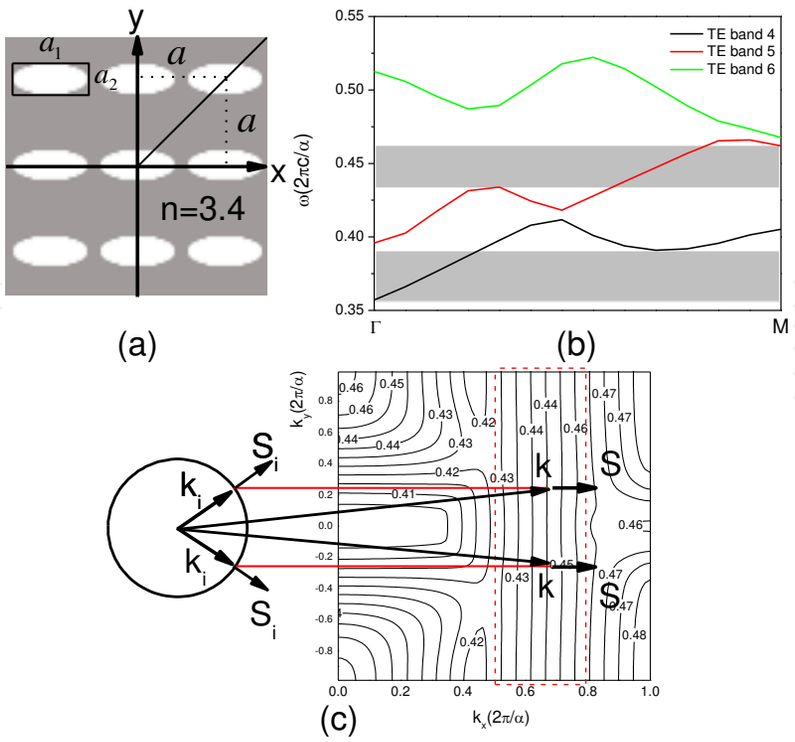

Figure 17. a) Schematic of the PC structure formed by a square lattice of elliptical holes; (b) band diagram of the fourth, fifth and sixth TE bands; (c) EFS contours of the fifth TE band [49].

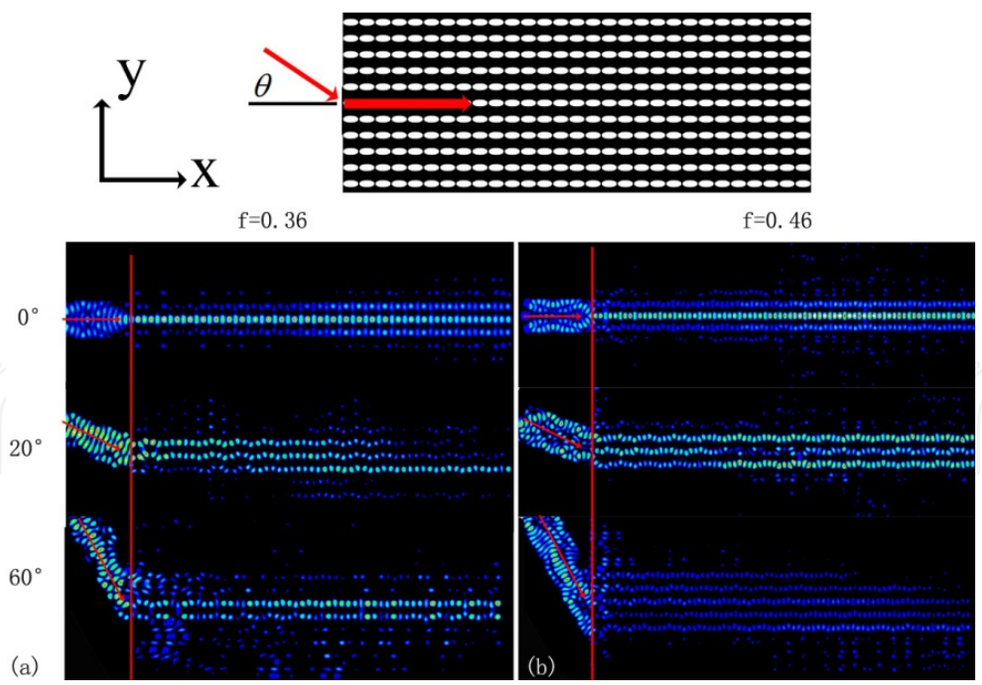

Figure 18. Electric field intensity distribution with 0°, 20° and 60° incident angles at the minimum normalized frequency 0.36 (a) and the maximum 0.46 (b). A FDTD method is used in the simulations [49].

simulations. We believe that this kind of structure may have potential applications in beam combiners and multiplexers.

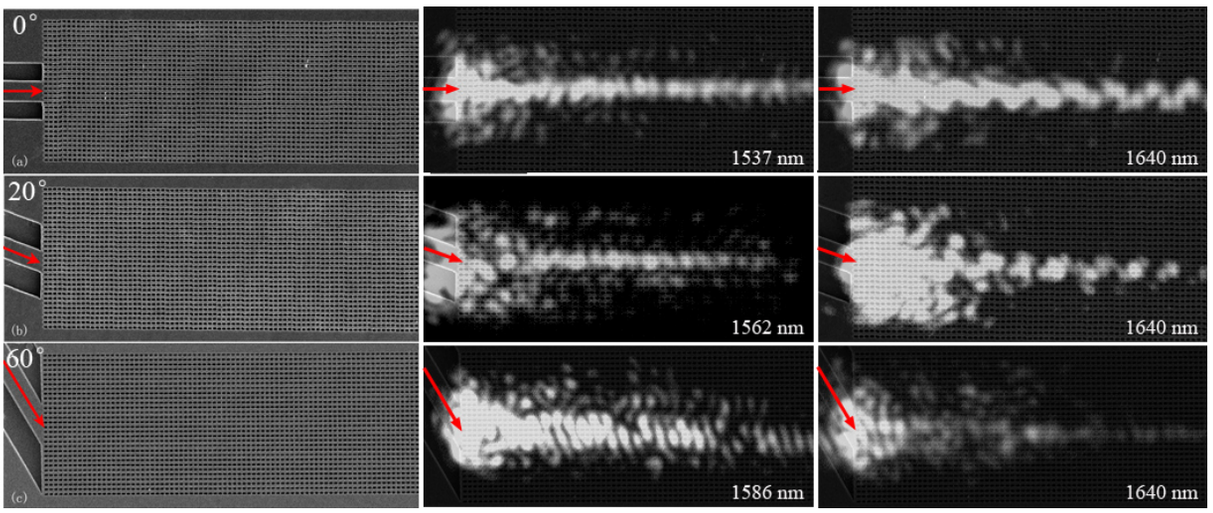

Figure 19. Left panels: SEM pictures of designed PC structures with 0° (a), 20° (b) and 60° (c) incident waveguide. Middle and right panels: Ray trace of light beam observed using IR camera and a high numerical aperture (NA = 0.50) objective. The patterns of the minimum and maximum wavelengths are shown for each incident angle [49].

6. On–chip wavelength–scale optical diode and isolator

Optical isolation is a long pursued object with fundamental difficulty in integrated photonics. The need to overcome this difficulty is becoming increasingly urgent with the emergence of silicon nano-photonics, which promises to create on-chip large-scale integrated optical systems. Motivated by the one-way effect, considerable effort has been dedicated to the study of unidirectional nonreciprocal transmission of electromagnetic waves, showing important promise in optical communications. Until now, on-chip integration of optical diode still stays in theory, particularly in silicon. These "optical diodes" include fluorescent dyes with a concentration gradient, absorbing multilayer systems, and second harmonic generators with a spatially varying wave vector mismatch. An electro-tunable optical isolator based on liquid-crystal heterojunctions, showing nonreciprocal transmission of circularly polarized light in photonic bandgap regions, has been reported. In another configuration using liquid crystals, linearly polarized light is used. In addition to many attempts on magneto-optical materials, optical isolators have also been fabricated using nonlinear optical processes and electro-absorption modulators.

An efficient routine to create optical diode is via time-reversal symmetry breaking or spatial inversion symmetry breaking [50], which could lead to the optical isolation in any device where the forward and backward transmissivity of light is very much different. We have reported a method for making unidirectional on-chip optical diodes based on the directional bandgap difference of two 2D square-lattice photonic crystals comprising a heterojunction structure and

the break of the spatial inversion symmetry. Simulations confirm the existence of a clear isolation effect in the designed heterojunction structure. We fabricate these on-chip optical diodes in silicon and the near-infrared experiment results show high-performance optical isolation, in good agreement with the theoretical prediction [51]. This device may play the same basic role in photonic circuits as the electrical diode does in electronic circuits. It could further pave the way to achieve on-chip optical logical devices without nonlinearity or magnetism and bloom the photonic network integration.

Figure 20(a) shows the schematic configuration of the original diode structure under study, which consists of two PC slab domains (PC1 and PC2) with the same lattice constant a but different air hole radii (r_1 and r_2, respectively) comprising a heterojunction structure. These two PC regions stand at a silicon slab [grey area in Fig. 20(a)]. Each PC region has a square-lattice pattern of air holes [white holes in Fig. 20(a)], with the hetero-interface between PC1 and PC2 along the Γ-M direction. We set the two hole radii as a fixed ratio to the lattice constant a, which are r_1=0.24a and r_2=0.36a in order to simplify our discussion. These two composite PCs would comprise a pure PC region if r_1=r_2. The light source is placed symmetrically aside the structure with two 4a-wide ridge waveguides connecting the surface of the two PC regions. The whole area is surrounded by a perfectly matched layer.

We simulated the transmission spectra for a TE-like light signal transporting along the forward (from left to right) and backward (from right to left) direction. The refractive index of the dielectric slab was set to 3.4, corresponding to that of silicon at 1,550 nm. The slab thickness was h=0.5a. Figure 20(b) shows the calculated forward (black line) and backward (red line) transmission spectra. The frequency is normalized by a/λ. It is clearly seen that there exists an isolation band ranging from 0.2649 to 0.2958 (a/λ), where the forward transmission forms a peak with a transmissivity of about 6% while the backward transmissivity is down between 0.5% and 1%. The forward peak is located at 0.2793 (a/λ), just in the middle of the isolation band. We define S=(T_F-T_B)/(T_F+T_B) as the signal contrast of the diode, where T_F and T_B denote the forward and backward transmissivity, respectively. The maximum S of this original diode equals 0.846 at the peak. Besides, there exists another isolation region from 0.2196 to 0.2649 (a/λ), where the backward transmissivity is higher than the forward transmissivity. This structure thus shows an extraordinary phenomenon of unidirectional transport property.

We calculated the band diagram of the TE-like modes of these two PC slabs using the 3D-FDTD method. Figures 21(a) and 21(b) show the calculation results. The first band (even mode) in bulk PC2 [Fig. 2(b)] is directional as the top mode frequency in the Γ-X direction (x-axis) is 0.2345 (a/λ) but that in the Γ-M direction (45°-direction) is 0.3087 (a/λ). Inside the region between 0.2345 (a/λ) and 0.3087 (a/λ), the all-directional transparent region of PC1 needs to be above 0.2633 (a/λ) [Fig. 21(a)] in order to match the bottom mode frequency in the Γ-X direction of the second band (odd mode). These two modes in PCs are the basic working mode of the diode structure. Here the even and odd modes are defined with respect to the off-slab mirror-reflection symmetry σ_z of the field component E_y. In the region between 0.2633 (a/λ) and 0.3087 (a/λ) PC1 is transparent in all directions, while PC2 is transparent along the Γ-M direction but opaque along the Γ-X direction. Compared with Fig. 20(b), the unidirectional transport region [0.2649 to 0.2958 (a/λ)] just coincides with the overlapped region between the directional bandgap of PC2 and the all-directional pass band of PC1. This simple picture indicates that

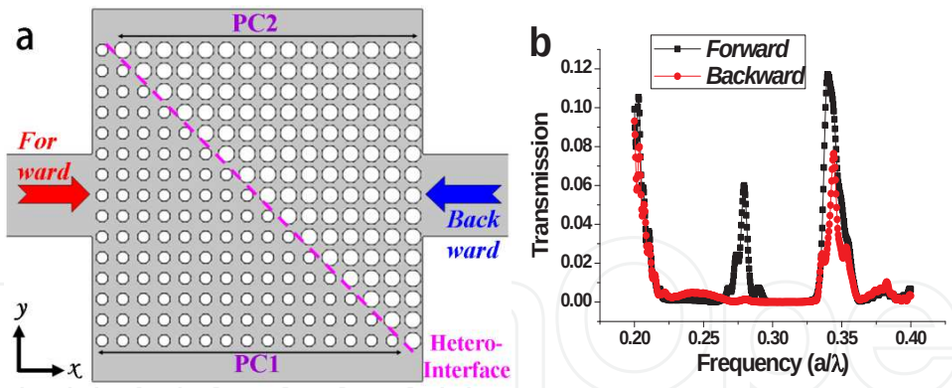

Figure 20. a) Schematic geometry of an original heterojunction optical diode formed by the interface (normal to the Γ-M direction) between two PC slabs (denoted as PC1 and PC2) with different hole radii (r_1 and r_2, respectively). (b) Simulated transmission spectra of the diode in the forward direction (the black line) and the backward direction (the red line). An input and output ridge waveguide has been used in the 3D-FDTD calculation. [51].

the current unidirectional transport effect involves two ingredients: (I) directional bandgap of PC2 and (II) all-directional pass band of PC1. Noting that the structure does not obey the spatial inversion symmetry alone the propagating direction, the principle of optical isolation can thus be summarized as follows:

1. Forward. When light goes across PC1 as the odd mode and reaches the hetero-junction along the Γ-X direction, it cannot stay in the Γ-X direction in PC2 further because of the Γ-X directional gap. But the hetero-junction is along the Γ-M direction, so light turns to the hetero-junction and diffracts as the even mode at any Γ-M direction into PC2, which passes through PC2 and eventually outputs.

2. Backward. When light goes directly into PC2 as the even mode, it turns to the two Γ-M direction paths which cannot convert to the odd mode of PC1 in the Γ-X direction and eventually leak out so that it does not output.

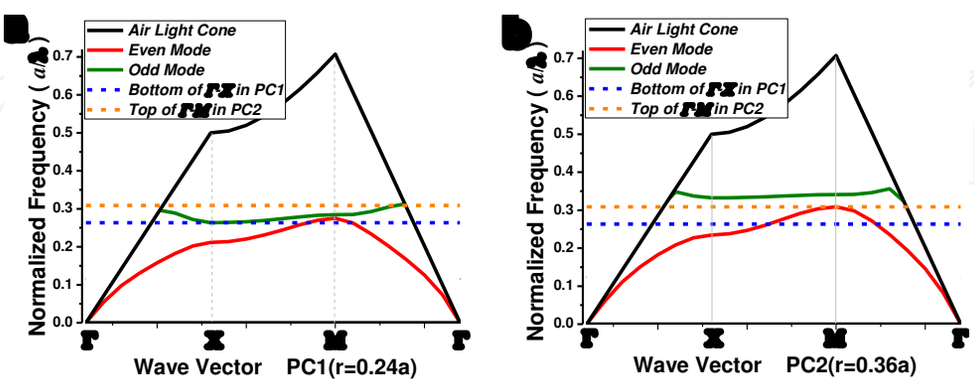

Figure 21. a) Calculated modal dispersion curve for PC1 (r=0.24*a*). (b) Calculated modal dispersion curve for PC2 (*r*=0.36*a*), in which the black line is the air light cone. The red curve denotes the first even mode, while the green curve denotes the second odd mode. The blue dashed line denotes the bottom frequency of the Γ-X directional odd mode [0.2633 (*a*/λ)] of PC1 and the orange dashed line denotes the top frequency of the Γ-M directional even mode of PC2 [0.3087 (*a*/λ)] [51].

Based on the numerical analysis of the optical diode, we have fabricated the original diode structure as well as a revised diode structure (with better performance) in silicon, whose SEM pictures are displayed in Fig. 22(a) and (c), respectively. Figures 22(b) and 22(d) show the theoretical and experimental results of the transmission spectra of the two diodes in the forward and backward directions. In Fig. 22(b) the theoretical forward peak of the original diode structure is at 1,575 nm [0.2793 (a/λ)] and the maximum transmissivity is 6%. The experimental forward peak is at 1,556 nm and the maximum transmissivity is 7%. In Fig. 22(d) the experimental forward peak is at 1,534 nm and the maximum transmissivity is 10% for the revised diode, whereas the theoretical forward peak is at 1,552 nm [0.2834 (a/λ)] with a transmissivity of 13%. The measured signal contrast S equals 0.718 (the original structure) and 0.831 (the revised structure) at the peak frequency. Both experimental peaks in Figs. 22(b) and 22(d) have a nearly 20 nm shift and 50 nm broadening against the theoretical simulations, which is probably due to the imperfections in fabrication. The experiment confirms the existence of the unidirectional transport effect in agreement with the theoretical prediction. Due to the arbitrariness of the lattice constant a, we can freely adjust the working frequency to anywhere as desired. This could be more convenient for the design of realistic photonic devices.

The principle for optical diode as analyzed in the above is robust as it is based on a simple directional bandgap mismatch effect of photonic crystal heterojunction. Yet, it should be noticed that in Figs. 22(b) and 22(d) the backward transmissions are fluctuating within 1% to 2% and both are higher than the simulation values, as a result, the signal contrast S degrades from 0.846 for the original structure and 0.92 for the revised structure in theory to 0.718 for the original structure and 0.831 for the revised structure in experiment. The performance improvement of the diode relies on how to maximize the peak of the forward transmissivity and minimize the backward transmissivity in experiment. Several means can help improve the forward transmissivity. First, one can change the air hole size of PC1 and PC2 and enlarge the directional bandgap. Calculations show that the forward peak transmissivity of the revised structure with r_1 =0.30a and r_2 =0.45a grows up dramatically to 29.4% while maintaining the same low level of backward transmissivity. Second, one can change the relative size of the input and output waveguides. Calculations show that by changing the input waveguide width to 2a and keeping the output waveguide width 4a, the forward peak signal increases up to 20.8% in transmissivity.

To reduce the backward transmissivity, one can either enlarge the directional bandgap of PC2 to attenuate the backward signal more strongly, or eliminate the return of leak-out light from the outside of slab or the structure boundary by introducing the absorbing metal dots near the structure, or enlarge the heterojunction structure appropriately so that the leak-out light cannot enter the output waveguide. Following the above general ideas, we further optimize the optical diode structures as illustrated in Fig. 23. The structure has parameters of r_1=100 nm and r_2=160 nm, and the input and output waveguide width are 2a and 6a, respectively. In experiment, we have got an optical diode with an maximum of 32.8% of the forward peak transmissivity and 0.885 of the signal contrast S at 1,557 nm.

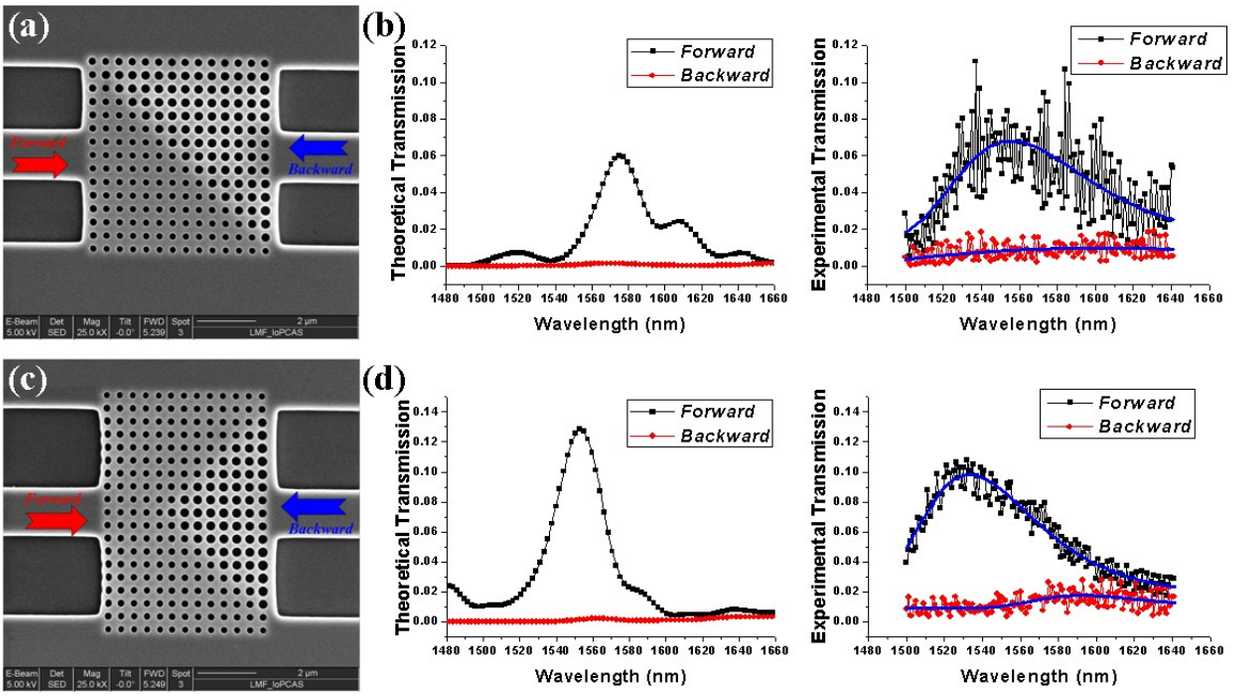

Figure 22. a) Scanning electron microscope images of the original optical diode structures. (b) Theoretical (left)and experimental (right) transmission spectra of the original diode structure. (c) Scanning electron microscope images of the revised optical diode structures. (d) Theoretical (left) and experimental (right) transmission spectra of the revised diode structure [51].

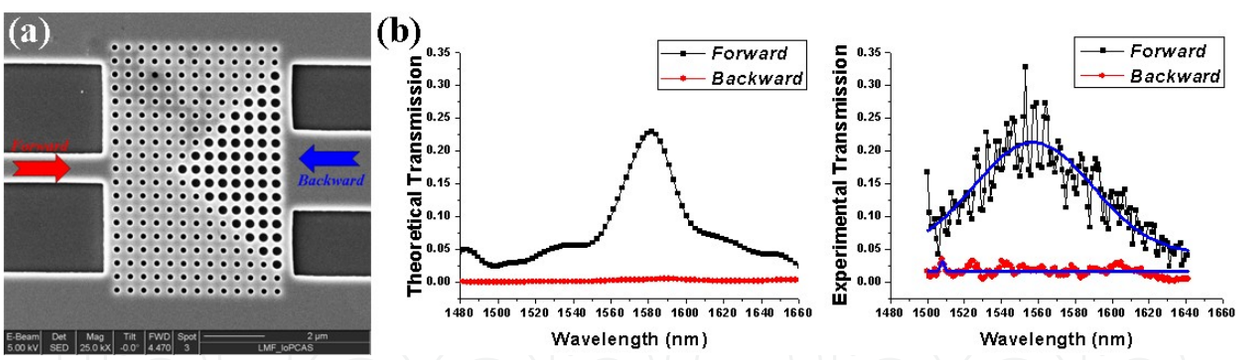

Figure 23. a) Scanning electron microscope images of the optimized optical diode system. (b) Theoretical (left) and experimental (right) transmission spectra of the optimized diode structure [51].

Our PC heterojunction diode has advantages of high signal contrast, wavelength-scale small sizes, and being all-dielectric, linear, and passive. Furthermore, it has a much smaller scale than those based on diffraction gratings and thus greatly facilitates large-scale integration. The high performance on-chip optical diode realized in silicon without nonlinearity or magnetism will stimulate the exploration of other more complex on-chip optical logical devices with ultra-high stability, integration and much less power consumption. Such an optical diode may play the same basic role in photonic circuits as the electrical diodes do in electronic circuits, which have significantly revolutionized fundamental science and advanced technology in various aspects of our routine life due to their capability of rectification of current flux. Furthermore,

its large-scale fabrication could be readily achieved by the well-developed CMOS techniques. The realization of high-performance on-chip optical diodes may open up a road toward photonic computers.

Strictly speaking, the existence of unidirectional transport effect of light does not mean automatic achievement of optical isolation. Recently there have appeared hot controversies upon whether isolation of light can be realized via linear and passive photonic structures. Several schemes to realize unidirectional transport of light through linear and passive photonic structures have been proposed, which are essentially based on the principle of spatial-inversion symmetry breaking. Feng *et al.* reports a passive silicon optical diode based on one-way guided mode conversion [52]. However, whether or not nonreciprocal transport of light can happen in the structure has raised hot controversies [53,54]. Fan *et al.* made a scattering matrix analysis for relevant forward and backward modes of the structure and argued that the structure is essentially reciprocal and cannot enable optical isolation because it possesses a symmetric coupling scattering matrix. In their response, Feng *et al.* acknowledge that their structure, as a one-way mode converter with asymmetric mode conversion, is Lorentz reciprocal, which states that the relationship between an oscillating current and the resulting electric field is unchanged if one interchanges the points where the current is placed and where the field is measured, and on its own cannot be used as the basis of an optical isolator. The controversies have thus raised a fundamental question: Can one construct an optical isolator by using a linear and time-independent optical system? The answer to this question by the authors of Ref. [53,54] obviously is no.

But our theoretical and experimental study on the optical isolation performance of our PC heterojunction diode leads to a totally different answer to the above question, namely, the spatial inversion symmetry breaking diode can construct an optical isolator in no conflict with any reciprocal principle [55]. To see whether there is a good isolation effect of the silicon diode, we implement a direct method that is originated from the conventional magneto-optical isolator that has been popularly used in laser devices [Fig. 24(a)]. One places a total reflection mirror after the output port in the forward direction of the isolator device and monitor the reflection signal from the input port. This reflection signal well describes and measures the round-trip transmissivity of light across the isolator device. If the reflection signal is the same as or is comparable with the forward signal, then the structure does not have the desired isolation property. In contrast, if the reflection signal is much smaller than the forward signal, then a good isolation property is implied.

An equivalent way to investigate the optical isolation performance of the diode structure is to adopt a doubled-diode structure with a mirror-symmetrical plane at the forward direction output port of the diode, as depicted in Fig. 25. Obviously this method has set all the forward output signals as the backward input signal of the diode and thus can directly test the isolation property of the diode structure. By implementing this method, we calculate simultaneously the forward transmissivity and the round-trip transmissivity of the diode structure. Comparison of these two quantities would directly measure their isolation properties. Figure 25(a) is the schematic geometry of the doubled-diode structure corresponding to the diode depicted in Fig. 24(b). The parameters of the diode are the same as in Fig. 23. The width of the input and

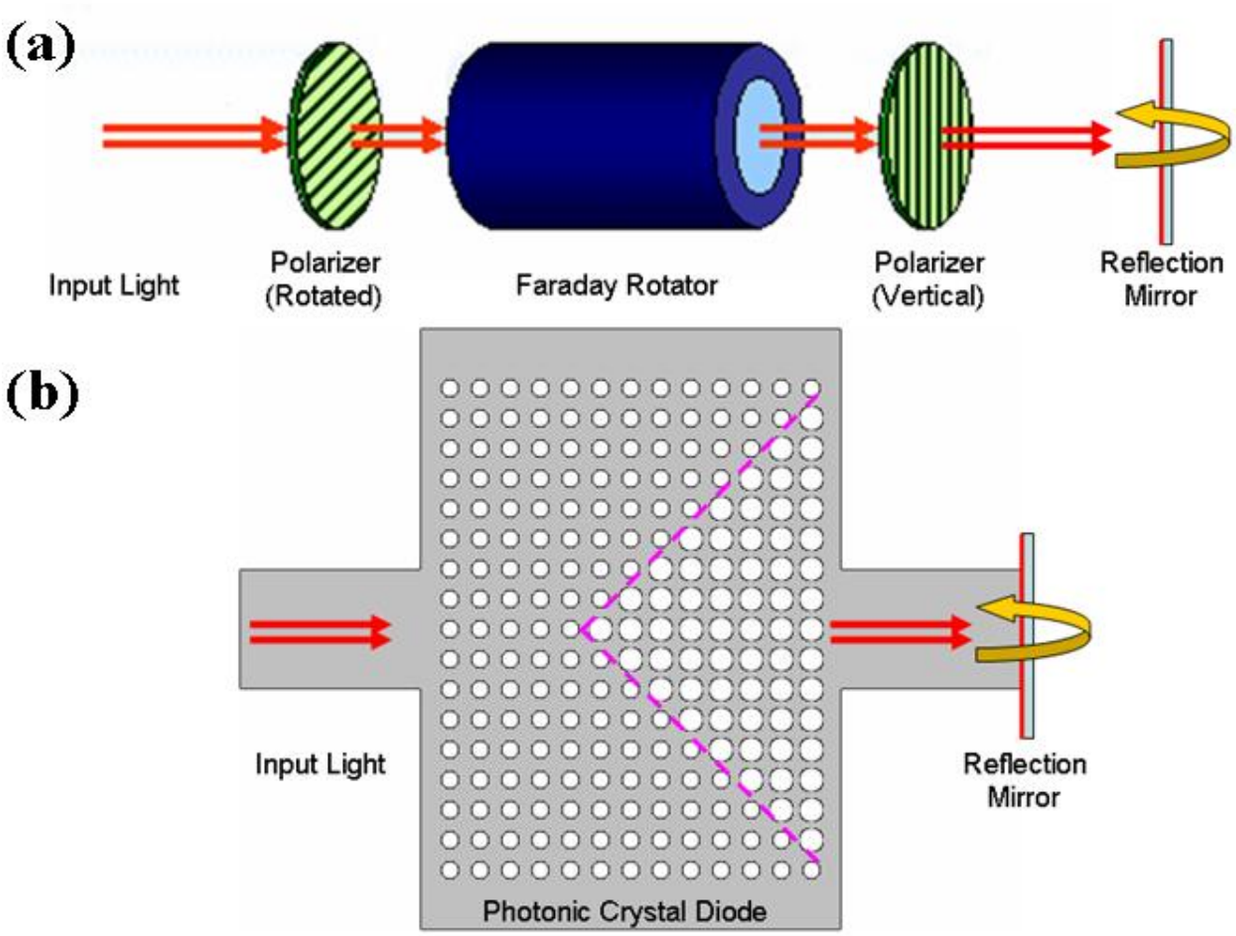

Figure 24. a) Traditional magnetic-optical isolator with reflection mirror at the output port. (b) On-chip optical diode system with reflection mirror at the output port. The absence of the reflection signal at the input port can indicate the isolation property of the system [55].

round-trip output waveguides is the same 2*a* (*a*=440 nm) and the center connection waveguide is 6*a*. The length of the center connection waveguide, which measures the distance of the total-reflection mirror away from the output port of the diode, is 10*a*. The spectra [Fig. 25(b)] show that the round-trip reflection peak is located at 1,582 nm and has a quantity of only 0.3%, which is almost two orders of magnitude smaller than the forward peak [with a maximum transmissivity of 22.9%]. The result indicates that the diode has a significant optical isolation property.

Based on the above numerical analysis, the double-diode structure was fabricated in silicon. Figure 25(c) shows the SEM images of the fabricated double-diode structures along the light path. The lattice constant *a* was 440 nm, and the radii r_1 and r_2 of air holes in the two photonic crystals of the heterojunction diode were approximately 110 nm and 160 nm. The length of the output waveguide is 4 μm (≈10*a*). The slab thickness was 220 nm. Figure 25(d) shows the experimentally measured forward and backward transmission spectra of the diode, as well as the round-trip transmission spectrum of the doubled-diode structure. The forward, backward and round-trip transmissions are optimized and the input/output loss has been removed. The

spectra show that the maximum round-trip transmissivity, located at 1,553 nm, is only 0.4%, almost two orders of magnitude smaller than the forward peak [with a maximum transmissivity of 32.9%]. The experiment confirms the existence of a significant isolation effect in agreement with the theoretical prediction. We change the length of the center connection waveguide of the double-diode structure from 4 μm to 3 μm and 5 μm. The measured round-trip transmission spectra for the three structures are displayed in Fig. 25(e). The results show that the round-trip transmission signal decreases remarkably along with the increasing length of the center connection waveguide, and already reaches an extremely low level (below 0.05%) in the whole spectrum range when the output waveguide length increases to 5 μm. This clearly indicates that the mode dispersion in the output waveguide of the diode has no influence to the isolation property of the diode. Due to the arbitrariness of the lattice constant *a*, we can freely adjust the isolation frequency to anywhere as desired. This could be very convenient for the design of realistic photonic devices.

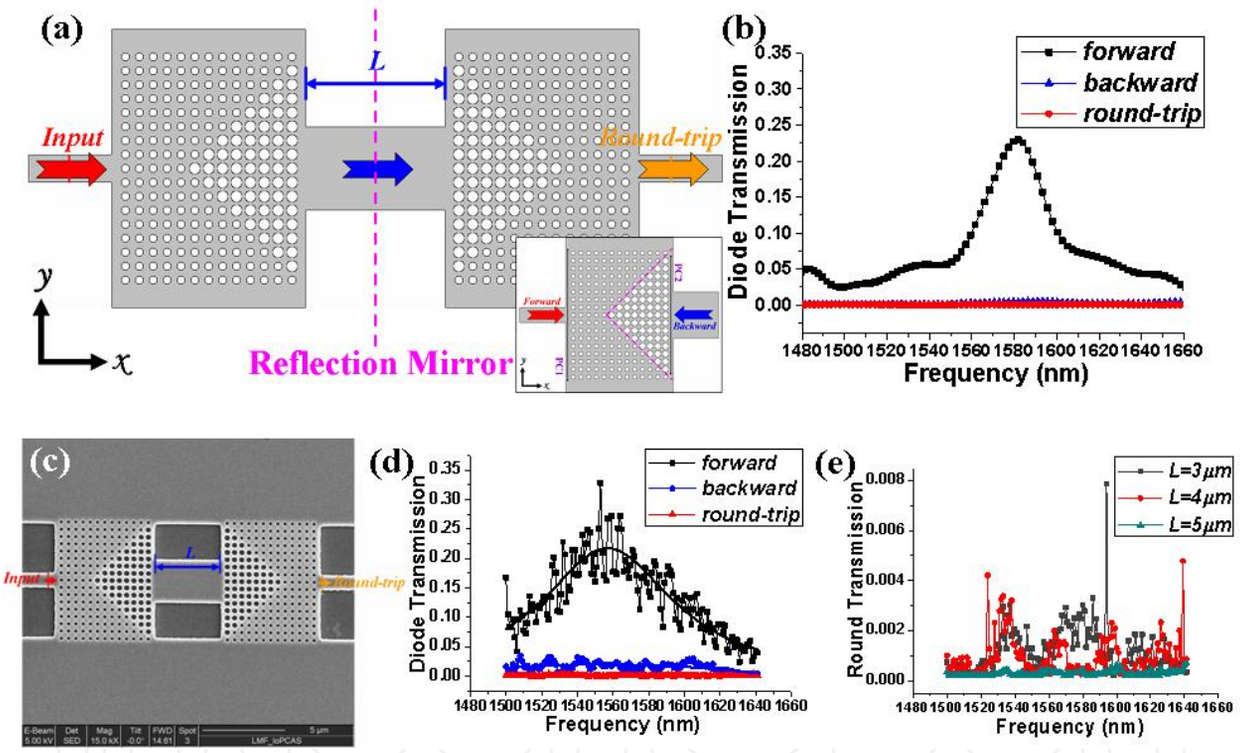

Figure 25. a) Schematic geometry of a doubled-diode structure with the total reflection mirror modeling the round-trip transmission of an isolator, and the corresponding single-diode structure under forward and backward transmissions. (b) Calculated forward (black line), backward (blue line), and round-trip (red line) transmission spectra of the diode. (c) Scanning electron microscope images of doubled-diode structure. (d) Experimental transmission spectra of forward transmission (black line), backward transmission (blue line), and the round-trip reflection (red line). (e) Experimental spectra of the round-trip reflection with changed center waveguide length L [55].

To better understand the underlying physics, we further make a detailed analyses based on the scattering matrix theory adopted in Ref. [53,54], and find that the above numerical results of optical isolation are in no conflict with the reciprocity theorem involved in our linear and passive silicon optical diode structure. Our diode basically consists of two in-plane information

channels (A and B, the input and output waveguide channels for infrared signal, which can be either single mode or multimode channels.) as well as many in-plane side-way and off-plane scattering channels (denoted as C as a whole, which causes dissipation of information away the signal channels). At the two ends of the diode device the fields are written as follows:

$$\begin{bmatrix} A_{out} \\ B_{out} \\ C_{out} \end{bmatrix} = S \begin{bmatrix} A_{in} \\ B_{in} \\ C_{in} \end{bmatrix}, \tag{3}$$

in which A_{in} corresponds to the input signal from port A, A_{out} to the output signal from port A, B_{in} to the input signal from port B, B_{out} to the output signal from port B, C_{in} to the input signal from port C, and C_{out} to the output signal from port C. The scattering matrix S transforms the input state of all the channels [the column vector in the right hand of Eq. (3)] into the output state of all the channels [the column vector in the left hand of Eq. (3)]. The scattering equation of the forward transmission is written as:

$$\begin{bmatrix} a_{out1} \\ b_{out1} \\ c_{out1} \end{bmatrix} = S \begin{bmatrix} a_{in0} \\ 0 \\ 0 \end{bmatrix}. \tag{4}$$

As the silicon diode structure is linear and passive, the system as a whole is reciprocal in regard to time-reversal symmetry following the Lorentz reciprocity theorem. As a result, the scattering matrix S is symmetric with $S = S^T$ and further satisfies:

$$S^* = S^{-1}. \tag{5}$$

Suppose all the output signals are reversed and come back into the system, then the input at port B for the system is now exactly the same as $\left[a^*_{out1} \quad b^*_{out1} \quad c^*_{out1}\right]^T$. The scattering equation is then

$$S \begin{bmatrix} a^*_{out1} \\ b^*_{out1} \\ c^*_{out1} \end{bmatrix} = (S^* \begin{bmatrix} a_{out1} \\ b_{out1} \\ c_{out1} \end{bmatrix})^* = (S^{-1} \begin{bmatrix} a_{out1} \\ b_{out1} \\ c_{out1} \end{bmatrix})^* = \begin{bmatrix} a^*_{in0} \\ 0 \\ 0 \end{bmatrix}, \tag{6}$$

which is exactly the same as the initial input from port A. This clearly indicates that there is no isolation behavior in the structure if all information is reversed back into the system, consistent with the reciprocity theorem for a time-reversal symmetric system.

However, the story can be very different when the in-plane signal transport is concerned, as is always the case for 2D silicon PC slab structures. In our structure the information and energy involved in C channels are dissipated permanently against the in-plane channel A and B due to scattering loss (both in-plane and off-plane), and they cannot be reversed back totally and input again into the structure, so in practice, C_{in} in Eq. (3) can be assumed to be zero. As a result, Eq. (6) should be modified as:

$$S\begin{bmatrix}0\\ b^*_{out1}\\ 0\end{bmatrix}=\begin{bmatrix}a_{out2}\\ b_{out2}\\ c_{out2}\end{bmatrix}. \tag{7}$$

In general, Eq. (7) looks very different from Eq. (6), which indicates that the reciprocal transport of light in regard to the signal channel A and B has been broken. It shows that even if the same forward transmission signal of port B is reversed back and input into the diode, the output signal of port A can be much different from the initial input signal a_{in0} of port A because no signal is reversed and input back into the channel C. Therefore, the considerable unidirectional transmission behavior can take place for the in-plane signal with no conflict with the reciprocal principle. In other words, the $a_{out2}(=S_{12}\bullet b^*_{out1})$ could be much different from $a^*_{in0}(=S_{11}\bullet a^*_{out1}+S_{12}\bullet b^*_{out1}+S_{13}\bullet c^*_{out1})$ when $S_{11}\bullet a^*_{out1}+S_{13}\bullet c^*_{out1}\neq 0$. This justifies the occurrence of a good isolation effect in the silicon optical diode. In ideal structures, both of them are zero, and Eq. (7) becomes

$$S\begin{bmatrix}0\\ b^*_{out1}\\ 0\end{bmatrix}=\begin{bmatrix}0\\ 0\\ c_{out2}\end{bmatrix}, \tag{8}$$

which implies a 100% signal contrast of the isolator.

It is worth saying a few more words here for better drawing a clear picture about the physics discussed in the above. In nature, as time always flows forward and cannot be reversed, one usually uses the term of reciprocal or nonreciprocal transport of light to describe a model system of back transport of light, in many cases to describe the reflection of light back into the considered structure. In this regard, simply consider a point source radiating an outgoing spherical wave front. If time can be reversed, the outgoing spherical wave front is contracted into an ingoing spherical wave front, eventually to a point. This is a very good picture to describe reciprocal transport of light in a linear system. However, to realize in real world such a concept, one needs to place a perfect spherical mirror concentric with the point source of light, which reflects back all information carried by the outgoing expanding spherical wave into the ingoing contracting spherical wave. If, however, one has only a small planar mirror placed at some distance and with a limited solid angle with respect to the source, the reflected

signal can never return to the initial state of a point source when it reaches the position where the light source is located. The conventional magneto-optical isolator also works in this category of physical picture. It is used to block down the back-reflection signal of the transmission light, and the underlying physics can be well described by the model of time-reversal symmetry breaking. The same physics picture applies equally well to our optical diode. The fact that there exists information dissipation from the signal channels to other channels in a spatial-inversion symmetry breaking structure is sufficient to induce an optical isolation in regard to the signal.

The above numerical calculations and experimental results have shown that our silicon PC slab heterojunction diode exhibits promising performance of optical isolation, with a round-trip transmissivity two orders of magnitude smaller than the forward transmissivity for in-plane infrared light across the structure. Our scattering matrix analysis indicates that the considerable unidirectional transport of in-plane signal light can be attributed to the information dissipation and selective modal conversion in the multiple-channel spatial-inversion symmetry breaking structure and has no conflict with reciprocal principle for a time-reversal symmetric structure. It is expected that optimized connection interfaces between the input and output waveguides with the heterojunction diode can yield better impedance mismatch and bring higher forward transmission efficiency. That optical isolation can occur in a linear, passive, and time-independent optical structure would stimulate more thinkings and insights on the general transport theory of light in the fundamental side and open up a road towards photonic logics in silicon integrated optical devices and circuits in the application side.

7. Parallel–hetero photonic crystal structures

Photonic crystal heterostructures (PCHs) have attracted increasing interest in optical integrated circuits and cavity quantum electrodynamics (cavity QED) due to their useful photonic band-gap structure and the ability to provide nanocavities with ultra-high quality factor (Q factor). The properties of PCHs have been investigated both in theory and experiment over the past several years. In previous works, the transmission and reflection characteristics of PCHs were revealed only across the hetero-interface between two photonic crystals with different lattice constants. The basic character of PCHs was the shift of the band edge, which results in a transmission gap with approximately 100% efficiency [56]. In comparison, recently we have reported a method for making a parallel-hetero perturbation inside the waveguide and analyze the optical properties of the photonic crystal parallel-hetero perturbation (PHP) structure. It is expected that this new type of PCHs not only contains the band-edge shifting property but also has an additional transmission gap which can be easily regulated in the middle of the transmission band. Simulations and experiments confirm the existence of the additional transmission gap [57]. Our work can help to enlarge the usage of PCHs in the design and fabrication of novel cavities and filters via localized modulation of structural dispersion, which are key components in a photonic network. Based on the PCH structures, we have further proposed and realized a new scheme of cavity, an interface heterostructure cavity without any confinement barrier to confine light. Interestingly, the localized resonant mode

lies in the pass band of the waveguide, in comparison of those cavities whose localized modes are always located within the band gap of the structures.

Figure 26(a) shows the geometry of the designed cavity, which consists of two identical parallel-hetero perturbation (PHP) waveguides. Each PHP waveguide consists of two semi-infinite PC (PC1 and PC2) slabs having slightly different lattice constants (a_1 and a_2, respectively). We assume a_2 is 5% larger than a_1. Each PC region has a triangular-lattice pattern of air holes, with the W1 waveguide formed by a line of missing holes along the Γ-K direction. Without periodicity along any direction, the PHP is essentially a kind of incommensurate PC superlattice along the waveguide direction. The transmission spectra of PHP waveguide structure exhibits an additional gap [0.29-0.30 (a_1/λ)] in the middle of the pass band of the two individual W1 waveguides besides the usual band edge shifting [0.26-0.27 (a_1/λ)] [56]. Figure 26(b) shows the calculated resonance spectrum of the cavity by using 3D FDTD method in association with the Pade approximation for the TE-like modes of the PC slab [58]. The resonance spectrum shows that a resonant mode surprisingly appears in the pass band region of the two PHP waveguides at 0.2855 (a_1/λ). In addition, this resonant mode (called band-pass mode) has a rather high value of Q factor reaching 5,340.

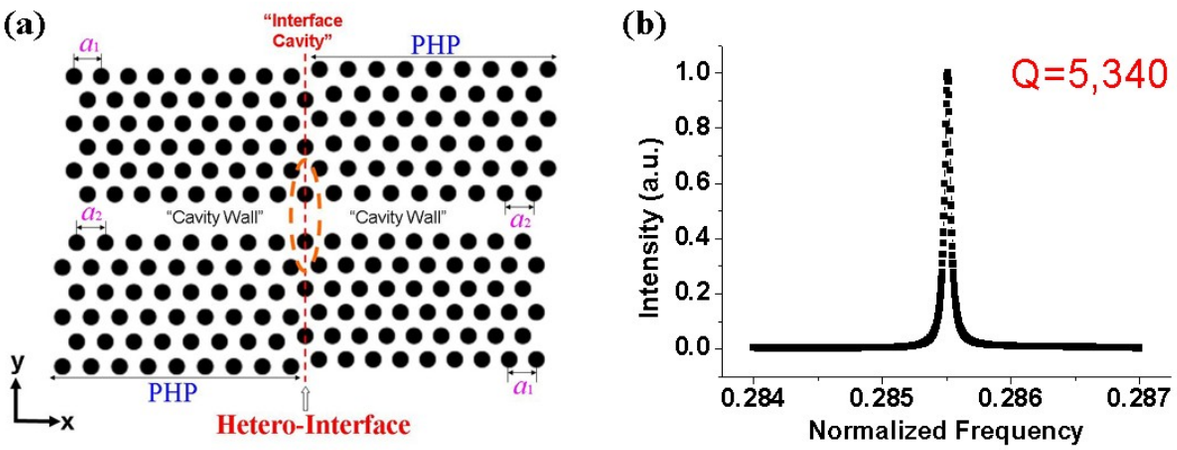

Figure 26. a) Schematic geometry of an anti-symmetric parallel-hetero cavity structure formed by only two PHP waveguides. (b) Calculated resonant mode distribution of the interface PHC [58].

We calculated the E_y field distribution of TE-like mode transporting along the waveguide at the resonance frequency 0.2855 (a_1/λ). It is surprising that the interface PHC has no influence on the propagation of waveguide mode [Fig. 27(a)]. To further confirm that the resonant mode really exists, we plot in Fig. 27(b) the calculated Ey field distribution of the resonant mode at the interface PHC at 0.2855 (a_1/λ) using a point source located within the interface cavity region. The mode does oscillate as a quadrupole form without barriers along the propagation direction even after the light source is turned off. This indicates that the resonant mode does exist and is not a calculation fault.

Based on the numerical analysis, an interface PHC structure was fabricated [Fig. 28(a)].The experimental results [Fig. 28(b)] confirms the theoretical prediction with the Q factor of the

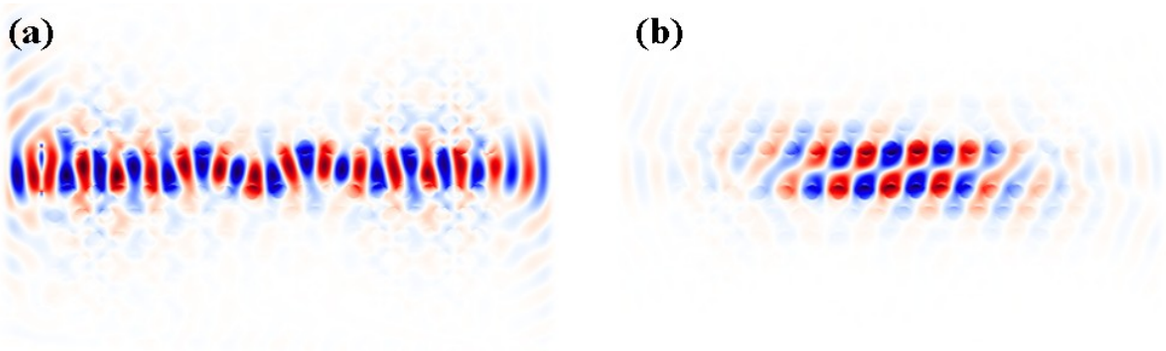

Figure 27. a) Calculated TE-like mode Ey field distribution of light transporting along the waveguide at the resonance frequency 0.2855 (a_1/λ). (b) Calculated TE-like mode Ey field distribution of the interface-cavity resonance at the resonance frequency 0.2855 (a_1/λ) [58].

cavity resonant mode decreases to 1,517 (centered at 1,570.2 nm) [Fig. 28(c)]. We then use an infrared CCD camera to monitor the resonant properties on top of the interface PHC region. When the laser wavelength is tuned to 1,570 nm, we can readily see a bright light spot located at the exact interface position [red circle in Fig. 28(d)] besides the other two light spots induced by the coupling between PHP waveguide and ridge waveguide. When the laser wavelength is tuned to 1,560 nm, the light spot in the red circle is gone while the other two light spots remain, indicating that the cavity is off resonance. This confirms the existence of the band-pass resonant mode.

The physics of PHC can be understood from the point of view of slow light effect. We have used a narrow light pulse centered at 0.2855 (a_1/λ) to pass through the interface PHC and a pure, same-length PHP waveguide, respectively, and recorded the output time of the pulse. The interface PHC is 599.25 time units, while the pure PHP waveguide is 606.3 time units, slightly longer than the interface PHC [Fig. 29(a)]. This indicates that the interface still contains one PC period length, so the whole interface PHC can be seen as a three-part structure, a combination of "slow light"–"fast light"–"slow light" region [Fig. 29(b)]. The central fast region in the PHC, which is only one period long, could also confine energy between two slow light regions and behaves as a cavity.

The physics underlying the interface PHC can also be analyzed by focusing on the phase shift in the waveguide of the interface PHC during propagation due to the fact that this band-pass mode is near the edge of the additional-gap region. The current PHC, which is made from an incommensurate superlattice structure, is similar to a periodic structure with dislocations. As a result, multiple scattering of light around the dislocation will occur and result in pinning effect of light (energy shifting across the dislocation line). Previous study shows that the PHP structure provides the asymmetric phase condition during the light propagation along the waveguide. The interface connects two same anti-symmetric PHPs and can be seen as a vertical edge dislocation line (phase reversal line), so that the phase condition is reversed to the opposite aside the interface. In material science the dislocation could cause the charge accumulation. Similarly our phase reversal dislocation gives an abrupt phase shift across the interface and may cause the photon accumulation around the phase reversal line. This phase

http://dx.doi.org/10.5772/55041

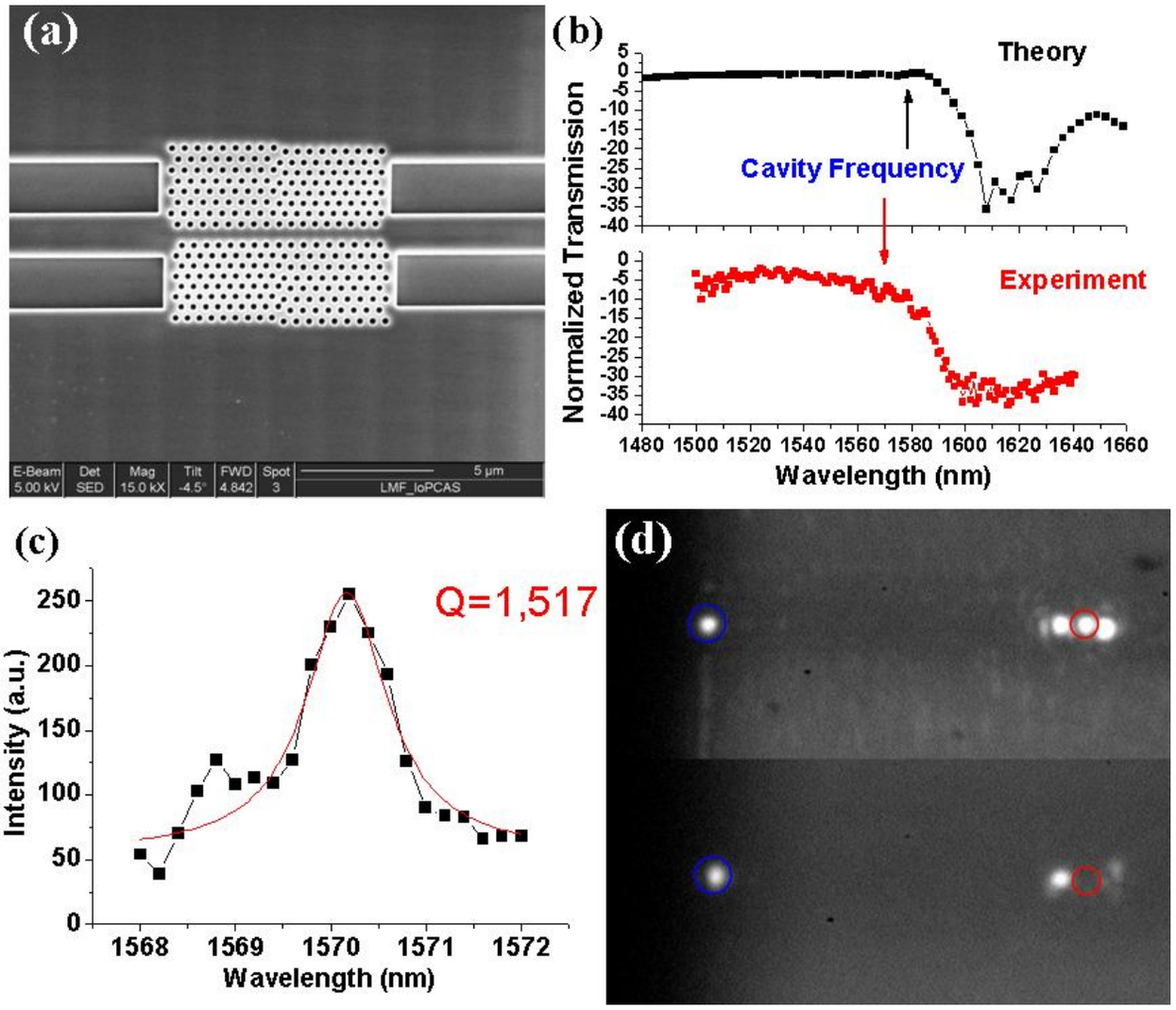

Figure 28. a) SEM image of the fabricated interface PHC composed of two PHP waveguides. (b) Experimental transmission spectrum of the interface PHC compared with the simulation results. (c) Resonance spectrum of the light spot obtained by its gray class analysis. (d) Infrared CCD images of the interface PHC structure on resonance (1,570 nm) and off resonance (1,560 nm) with output ridge waveguide [58].

reversal dislocation plays as a defect and forces the light energy distribution to become skew and swinging while crossing the interface [Fig. 27(a)]. The local energy oscillation acts as the cavity resonance and leads to the photon accumulation at the interface.

The PHC has several distinct properties. First, unlike the conventional PC cavities which are formed either by removing one or several air holes or by waveguide-like hetero-cavities, the current PHC does not have any confinement barrier to confine light. Second, the resonant mode is located within the pass band of waveguides, so the localized resonant mode and the continuous waveguide mode can easily co-exist in the same frequency and space regime. Third, the coupling efficiency between waveguide and cavity modes is much higher than the conventional cavities, which strongly depend on the transverse evanescent field profile overlap of the cavity mode and the waveguide mode. As a result, this PHC has nearly no

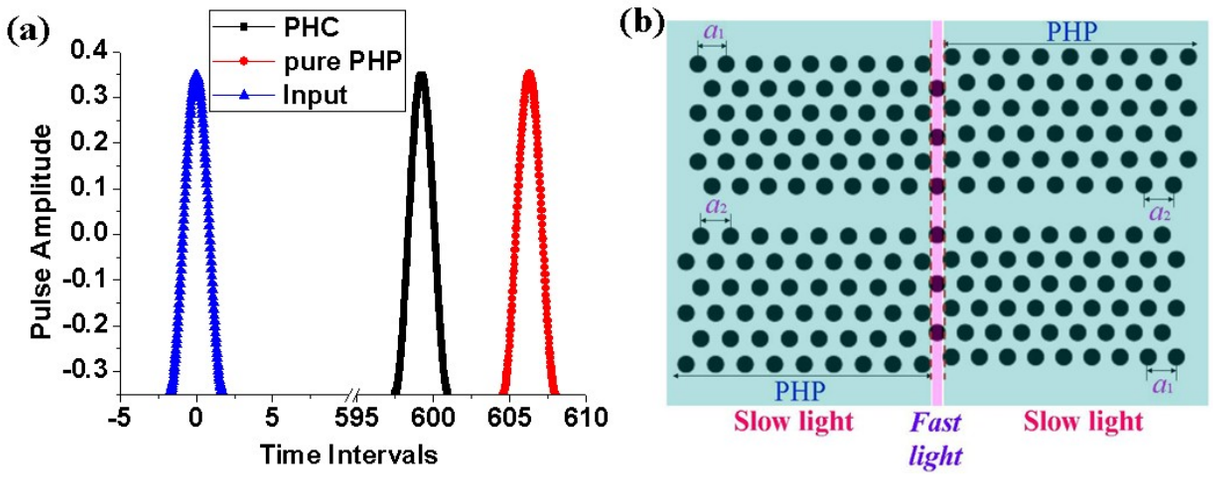

Figure 29. a) Time diagram of a narrow light pulse at 0.2855 (a_1/λ) passing through the interface PHC and a pure, same-length PHP waveguide. (b) Schematic slow light diagram of interface PHC [58].

influence on the propagation of waveguide mode despite the presence of localized cavity mode. High coupling efficiency between waveguide and cavity mode can help to reduce the operating power for PC lasers, and make it possible to integrate multiple lasers, photodetectors, and switches on a single chip.

8. Conclusions

In summary, we have presented recent progresses on infrared 2D air-bridged silicon PC slab devices that were made in our group in the past several years. 2D air-bridged silicon PC slab structures can confine light by the high index contrast in the vertical off-plane direction and manipulate light by photonic band and band gaps in the lateral in-plane direction. In addition, silicon is transparent and has a large refractive index in the infrared wavelengths. Therefore, the air-bridged silicon PC structures become one of the most important elements in integrated optics.

In this review, we have discussed several integrated optical elements and devices in regard to their design, fabrication, and characterization. These devices are based on either the PBG or photonic band structure engineering. To bring these devices into reality, we have made extensive efforts to construct high-efficiency numerical simulation tools for solution of photonic band structures, transmission spectra, light propagation dynamics, light wave patterns, and many others. These simulations allow for design of optimized PC structures for a specific application. The fabrication of these devices strongly depends on state-of-the-art nanofabrication technologies including EBL, FIB, ICP etching, and other wet etching techniques and procedures. We have constructed a convenient experimental setup to measure the transmission spectra and monitor the propagation path of infrared signals within PC structures simultaneously. The setup makes the optical characterization of PC devices accurate, user-friendly, fast, and convenient.

http://dx.doi.org/10.5772/55041

We have proposed Γ−M waveguides made in 2D triangular-lattice PC slabs. After a series of optimization and improvement, we find out the optimized geometries for high performance wide band Γ−M waveguides. As the Γ−M waveguide is perpendicular to the usual Γ−K waveguide, we combine the Γ−K waveguide and Γ−M waveguide together to form 90° waveguide bends and channel drop filters. The combination of Γ−M waveguide and Γ−K waveguide can offer a flexible way to interconnect and couple between different devices. In addition, we have shown design of two other kinds of channel drop filters. They achieve fine tuning of the resonant wavelengths by changing the size of the cavities or the shape of the air holes around the cavities. We have also designed and realized PC waveguide based on the coupled-cavity scheme. There are a lot of geometric parameters to fine tune the light transport properties in the structure. Moreover, we have successfully fabricated high-Q silicon PC microcavities with a Q-factor up to 70000 and this paves the way to experimentally explore light-matter interaction within the strong-coupling regime in the all-solid platform.

We have investigated optical devices that work on band structure engineering. We have explored PC structures that exhibit interesting and useful dispersion and refraction properties, such as negative refraction and self-collimation effects. We have designed and fabricated a kind of PC structure with negative refraction effect and use SNOM technology to observe the negative refraction ray trace of infrared light beam. In addition, we obtain broadband large-angle self-collimation effect for TE-like guided modes in infrared wavelength.

We have demonstrated the design, fabrication, and characterization of on-chip wavelength-scale optical diodes that are made from the heterojunction between two different silicon 2D square-lattice PC slabs with directional bandgap mismatch and different mode transitions. The measured transmission spectra show considerable unidirectional transmission behavior, in good agreement with numerical simulations. The experimental realization of on-chip optical diodes with wavelength-scale size using all-dielectric, passive, and linear silicon photonic crystal structures may help to construct on-chip optical logical devices without nonlinearity or magnetism, and would open up a road towards photonic computers.

We have demonstrated optical isolation of our diode structure. Both numerical simulations and experimental measurements show that the round-trip transmissivity of our diode could be two orders of magnitudes smaller than the forward transmissivity, indicating good performance of optical isolation. The occurrence of in-plane light isolation is attributed to the information dissipation due to off-plane and side-way scattering and selective modal conversion in the multiple-channel structure and has no conflict with the reciprocal principle. That optical isolation can occur in a linear, passive, and time-independent optical structure would stimulate more thinkings and insights on the general transport theory of light in the fundamental side and open up a road towards photonic logics in silicon integrated optical devices and circuits in the application side.

We have designed and fabricated cavities without confinement barrier by combining two incommensurate PC superlattice waveguides. A resonant mode with a high quality factor shows up in the pass band of waveguides. It has nearly no influence on the propagation of waveguide mode and can be directly coupled with the waveguide mode. The experimental measurement confirms the theoretical prediction of extraordinary coexistence of localized

cavity mode and continuous waveguide mode with high coupling efficiency in the same frequency and space regime. The novel type of cavity has a number of unique properties that are advantageous to on-chip information transport and processing. The discovery of cavity without confinement barrier might attract interest in fundamental physics and optical engineering communities.

All of these results show that 2D air-bridged silicon PC structures can control light propagation in many flexible ways and have many potential applications in all-optical integrated circuits and other fields. The efforts that we have made and the experiences that we have accumulated in the past several years will allow us to design and realize PC devices with novel functionalities.

Acknowledgements

This work was supported by the National Key Basic Research Special Foundation of China (No. 2011CB922002), the National Natural Science Foundation of China, and National Center for Nanoscience and Technology of China. The authors would like to thank the previous members of our group, Cheng Ren, Haihua Tao, Yazhao Liu, and Changzhu Zhou for their contributions to the works presented in this review.

Author details

Zhi-Yuan Li*, Chen Wang and Lin Gan

*Address all correspondence to: lizy@aphy.iphy.ac.cn

Laboratory of Optical Physics, Institute of Physics, Chinese Academy of Sciences, Beijing, China

References

[1] Yablonovitch, E. Inhibited spontaneous emission in solid-state physics and electronics. Physical Review Letters, (1987).

[2] Joannopoulos, J D, Johnson, S G, Winn, J N, & Meade, R D. Photonic Crystals: Molding the Flow of Light. 2nd ed. Princeton: Princeton University Press, (2008).

[3] Valentine, J, Zhang, S, Zentgraf, T, Ulin-avila, E, Genov, D A, Bartal, G, & Zhang, X. Three-dimensional optical metamaterial with a negative refractive index. Nature, (2008).

[4] Yao, J, Liu, Z W, Liu, Y M, Wang, Y, Sun, C, Bartal, G, Stacy, A M, & Zhang, X. Optical negative refraction in bulk metamaterials of nanowires. Science, (2008).

[5] Johnson, S G, Fan, S H, Villeneuve, P R, Joannopoulos, J D, & Kolodziejski, L A. Guided modes in photonic crystal slabs. Physical Review B: Condensed Matter and Materials Physics, (1999).

[6] Painter, O, Lee, R K, Scherer, A, Yariv, A, Brien, O, Dapkus, J D, Kim, P D, & , I. Two-dimensional photonic band-gap defect mode laser. Science, (1999).

[7] Mcnab, S J, Moll, N, & Vlasov, Y A. Ultra-low loss photonic integrated circuit with membrane-type photonic crystal waveguides. Optics Express, (2003).

[8] Luo, C Y, Johnson, S G, Joannopoulos, J D, & Pendry, J B. All-angle negative refraction without negative effective index. Physical Review B: Condensed Matter and Materials Physics, (2002).

[9] Kosaka, H, Kawashima, T, Tomita, A, Notomi, M, Tamamura, T, Sato, T, & Kawakami, S. Self-collimating phenomena in photonic crystals. Applied Physics Letters, (1999).

[10] Yu, X F, & Fan, S H. Bends and splitters for self-collimated beams in photonic crystals. Applied Physics Letters, (2003).

[11] Kosaka, H, Kawashima, T, Tomita, A, Notomi, M, Tamamura, T, Sato, T, & Kawakami, S. Superprism phenomena in photonic crystals: toward microscale lightwave circuits. Journal of Lightwave Technology, (1999).

[12] Baba, T, Matsumoto, T, & Echizen, M. Finite difference time domain study of high efficiency photonic crystal superprisms. Optics Express, (2004).

[13] Berrier, A, Mulot, M, Swillo, M, Qiu, M, Thylén, L, Talneau, A, & Anand, S. Negative refraction at infrared wavelengths in a two-dimensional photonic crystal. Physical Review Letters, (2004).

[14] Born, M, Wolf, E, & Bhatia, A B. Principles of Optics: Electromagnetic Theory of Propagation, Interference and Diffraction of Light. New York : Cambridge University Press, (1999).

[15] Ho, K M, Chan, C T, & Soukoulis, C M. Existence of a photonic gap in periodic dielectric structures. Physical Review Letters, (1990).

[16] Johnson, S, & Joannopoulos, J. Block-iterative frequency-domain methods for Maxwell's equations in a planewave basis. Optics Express, (2001).

[17] Li, Z Y, Gu, B Y, & Yang, G Z. Large absolute band gap in 2D anisotropic photonic crystals. Physical Review Letters, (1998).

[18] Li, Z Y, Wang, J, & Gu, B Y. Creation of partial band gaps in anisotropic photonic-band-gap structures. Physical Review B: Condensed Matter and Materials Physics, (1998).

[19] Pendry, J B. Photonic Band Structures. Journal of Modern Optics, (1994).

[20] Chan, C T, Yu, Q L, & Ho, K M. Order-N spectral method for electromagnetic waves. Physical Review B: Condensed Matter and Materials Physics, (1995).

[21] Taflove, A. Computational Electrodynamics: the Finite-Difference Time-Domain Method. Boston : Artech House, (1995).

[22] Nicorovici, N A, Mcphedran, R C, & Botten, L C. Photonic band gaps for arrays of perfectly conducting cylinders. Physical Review E: Statistical Physics, Plasmas, Fluids, and Related Interdisciplinary Topics, (1995).

[23] Li, L M, & Zhang, Z Q. Muitiple-scattering approach to finite-sized photonic band-gap materials. Physical Review B: Condensed Matter and Materials Physics, (1998).

[24] Li, Z Y, & Lin, L L. Photonic band structures solved by a plane-wave-based transfer-matrix method. Physical Review E: Statistical, Nonlinear, and Soft Matter Physics, (2003).

[25] Li, Z Y, & Lin, L L. Evaluation of lensing in photonic crystal slabs exhibiting negative refraction. Physical Review B: Condensed Matter and Materials Physics, (2003).

[26] Lin, L L, Li, Z Y, & Ho, K M. Lattice symmetry applied in transfer-matrix methods for photonic crystals. Journal of Applied Physics, (2003).

[27] Li, Z Y, & Ho, K M. Light propagation in semi-infinite photonic crystals and related waveguide structures. Physical Review B: Condensed Matter and Materials Physics, (2003).

[28] Li, Z Y, Lin, L L, & Ho, K M. Light coupling with multimode photonic crystal waveguides. Applied Physics Letters, (2004).

[29] Che, M, & Li, Z Y. Analysis of photonic crystal waveguide bends by a plane-wave transfer-matrix method. Physical Review B: Condensed Matter and Materials Physics, (2008).

[30] Che, M, & Li, Z Y. Analysis of surface modes in photonic crystals by a plane-wave transfer-matrix method. Journal of the Optical Society of America a-Optics Image Science and Vision, (2008).

[31] Li, Z Y, & Ho, K M. Analytic modal solution to light propagation through layer-by-layer metallic photonic crystals. Physical Review B: Condensed Matter and Materials Physics, (2003).

[32] Li, J J, Li, Z Y, & Zhang, D Z. Second harmonic generation in one-dimensional nonlinear photonic crystals solved by the transfer matrix method. Physical Review E: Statistical, Nonlinear, and Soft Matter Physics, (2007).

[33] Li, Z Y, Li, J J, & Zhang, D Z. Nonlinear frequency conversion in two-dimensional nonlinear photonic crystals solved by a plane-wave-based transfer-matrix method. Physical Review B: Condensed Matter and Materials Physics, (2008).

[34] Oskooi, A F, Roundy, D, Ibanescu, M, Bermel, P, Joannopoulos, J D, & Johnson, S G. MEEP: A flexible free-software package for electromagnetic simulations by the FDTD method. Computer Physics Communications, (2010).

[35] Shinya, A, Mitsugi, S, Kuramochi, E, & Notomi, M. Ultrasmall multi-channel resonant-tunneling filter using mode gap of width-tuned photonic-crystal waveguide. Optics Express, (2005).

[36] Song, B S, Nagashima, T, Asano, T, & Noda, S. Resonant-wavelength tuning of a nanocavity by subnanometer control of a two-dimensional silicon-based photonic crystal slab structure. Applied Optics, (2009).

[37] Liu, Y Z, Liu, R J, Zhou, C Z, Zhang, D Z, & Li, Z Y. Gamma-Mu waveguides in two-dimensional triangular-lattice photonic crystal slabs. Optics Express, (2008).

[38] Zhou, C Z, Liu, Y Z, & Li, Z Y. Waveguide bend of 90° in two-dimensional triangular lattice silicon photonic crystal slabs. Chinese Physics Letters, (2010).

[39] Tao, H H, Ren, C, Liu, Y Z, Wang, Q K, Zhang, D Z, & Li, Z Y. Near-field observation of anomalous optical propagation in photonic crystal coupled-cavity waveguides. Optics Express, (2010).

[40] Hennessy, K, Badolato, A, Winger, M, Gerace, D, Atatüre, M, Gulde, S, Fält, S, Hu, E L, & Imamoglu, A. Quantum nature of a strongly coupled single quantum dot-cavity system. Nature, (2007).

[41] Akahane, Y, Asano, T, Song, B S, & Noda, S. High-Q photonic nanocavity in a two-dimensional photonic crystal. Nature, (2003).

[42] Zhou, C Z, Wang, C, & Li, Z Y. Fabrication and spectra-measurement of high Q photonic crystal cavity on silicon slab", Acta Physica Sinica, (2012).

[43] Ren, C, Tian, J, Feng, S, Tao, H H, Liu, Y Z, Ren, K, Li, Z Y, Cheng, B Y, Zhang, D Z, & Yang, H F. High resolution three-port filter in two dimensional photonic crystal slabs. Optics Express, (2006).

[44] Liu, Y Z, Feng, S A, Tian, J, Ren, C, Tao, H H, Li, Z Y, Cheng, B Y, Zhang, D Z, & Luo, Q. Multichannel filters with shape designing in two-dimensional photonic crystal slabs. Journal of Applied Physics, (2007).

[45] Liu, Y Z, Liu, R J, Feng, S A, Ren, C, Yang, H F, Zhang, D Z, & Li, Z Y. Multichannel filters via Γ-M and Γ-K waveguide coupling in two-dimensional triangular-lattice photonic crystal slabs. Applied Physics Letters, (2008).

[46] Gan, L, Liu, Y Z, Li, J Y, Zhang, Z B, Zhang, D Z, & Li, Z Y. Ray trace visualization of negative refraction of light in two-dimensional air-bridged silicon photonic crystal slabs at 1.55 μm. Optics Express, (2009).

[47] Nguyen, H M, Dundar, M A, Van Der Heijden, R W, Van Der Drift, E, Salemink, J M, Rogge, H W M, & Caro, S. J. Compact Mach-Zehnder interferometer based on self-collimation of light in a silicon photonic crystal. Optics Express, (2010).

[48] White, T P, De Sterke, C M, Mcphedran, R C, & Botten, L C. Highly efficient wide-angle transmission into uniform rod-type photonic crystals. Applied Physics Letters, (2005).

[49] Gan, L, Qin, F, & Li, Z Y. Broadband large-angle self-collimation in two-dimensional silicon photonic crystal", Optics Letters, (2012).

[50] Serebryannikov, A E. One-way diffraction effects in photonic crystal gratings made of isotropic materials. Physical Review B: Condensed Matter and Materials Physics. (2009).

[51] Wang, C, Zhou, C Z, & Li, Z Y. On-chip optical diode based on silicon photonic crystal heterojunctions. Optics Express, (2011).

[52] Feng, L, Ayache, M, Huang, J, Xu, Y L, Lu, M H, Chen, Y F, Fainman, Y, & Scherer, A. Nonreciprocal light propagation in a silicon photonic circuit. Science, (2011).

[53] Fan, S, Baets, R, Petrov, A, Yu, Z, Joannopoulos, J D, Freude, W, Melloni, A, Popovic, M, Vanwolleghem, M, Jalas, D, Eich, M, Krause, M, Renner, H, Brinkmeyer, E, & Doerr, C R. Comment on "Nonreciprocal light propagation in a silicon photonic circuit". Science, (2012). b.

[54] Feng, L, Ayache, M, Huang, J, Xu, Y L, Lu, M H, Chen, Y F, Fainman, Y, & Scherer, A. Response to comment on "Nonreciprocal light propagation in a silicon photonic circuit". Science, (2012). c.

[55] Wang, C, Zhong, X L, & Li, Z Y. Linear and passive silicon optical isolator. Scientific Reports, (2012).

[56] Song, B S, Asano, T, Akahane, Y, Tanaka, Y, & Noda, S. Transmission and reflection characteristics of in-plane hetero-photonic crystals. Applied Physics Letters (2004).

[57] Wang, C, Zhou, C Z, & Li, Z Y. Creation of stop band by introducing parallel-hetero perturbation in two-dimensional photonic crystal waveguides Journal of Optics, (2011).

[58] Wang, C, & Li, Z Y. Cavities without confinement barrier in incommensurate photonic crystal superlattices EPL, (2012).